From Light to Acetate: How Trophic Conditions Shape Growth and Cell Cycle Progression in *Chlamydomonas reinhardtii*

Rabinder Singh[1], Firas Louis[1], P. V. Sijil[1], Martín Mora-García[1], Bipasha Bhattacharjee[1], Kateřina Bišová[1]

[1] Laboratory of Cell Cycles of Algae, Centre Algatech, Institute of Microbiology of the Czech Academy of Sciences, 237, Trebon 379 01, Czech Republic

rabindersingh@alga.cz

Abstract

The unicellular green alga *Chlamydomonas reinhardtii* provides a tractable model for investigating how carbon availability influences metabolic organization and cell-cycle control in photosynthetic eukaryotes. Its capacity for autotrophic (light, CO_2), mixotrophic (light, CO_2, acetate), and heterotrophic (acetate, dark) growth enables systematic analysis of trophic-state-dependent regulation. We performed comparative transcriptomic analyses of strain 21gr grown under these three regimes at 30 °C. Mixotrophy resulted in the highest biomass accumulation and was associated with earlier cell-cycle commitment compared with autotrophy, whereas heterotrophy displayed delayed commitment and reduced growth. Transcriptomic profiling revealed coordinated upregulation of central carbon metabolic pathways under mixotrophy, including photorespiration, glycolysis, the oxidative pentose phosphate pathway, and tricarboxylic acid cycle functions, consistent with enhanced carbon flux and biosynthetic capacity. In contrast, heterotrophy preferentially induced acetate assimilation and glyoxylate cycle genes and was accompanied by elevated expression of cell-cycle regulators, including the CDK-inhibitory kinase WEE1. Together,

these findings indicate that trophic mode modulates the coupling between carbon metabolism and cell-cycle progression, with mixotrophy supporting integrated metabolic and proliferative activity, whereas heterotrophy is associated with delayed cell-cycle timing and transcriptional signatures of metabolic adjustment.

Keywords: autotrophy, mixotrophy, heterotrophy, cell cycle, cell division, commitment point, physiological responses, *Chlamydomonas*.

Introduction

The unicellular green alga *Chlamydomonas reinhardtii* is a genetically tractable model organism for investigating eukaryotic photosynthesis [1], cellular metabolism [2], and the cell cycle [3]. *C. reinhardtii* shares key pathways with other algae and land plants [4] and offers the advantages of a unicellular model with a fully sequenced haploid genome and robust genetic tools [5]. It can grow photoautotrophically using light as the sole energy source for carbon dioxide fixation, heterotrophically by utilizing acetate as a carbon and energy source, or mixotrophically by combining both light and acetate [6-8]. It grows easily at large scale and synchronizes with light/dark cycles, making it an ideal system for studying gene expression and cell division patterns [2]. Despite significant progress, there remains a substantial gap in our understanding of the biochemistry and regulatory mechanisms governing metabolic processes in *C. reinhardtii*, especially regarding how the cells reprogram their physiology in response to varying energy and carbon sources. Each trophic mode imposes distinct metabolic demands, influencing key cellular processes such as glycolysis/gluconeogenesis, the tricarboxylic acid (TCA) cycle, amino acid biosynthesis, energy storage, and cell cycle progression [9].

To assimilate C_2 compounds such as acetate, C. reinhardtii uses an ATP-dependent entry into the glyoxylate cycle, generating C_4 intermediates that can subsequently be converted into amino acids or soluble carbohydrates [10]. Acetate suppresses photosynthesis while enhancing respiration under light and air bubbling, potentially through increased alternative oxidase activity [11-14]. Acetate availability is linked to altered expression of nuclear-encoded, chloroplast-targeted light-harvesting proteins (LHCII chlorophyll a/b–binding proteins), with acetate promoting their accumulation in the dark and attenuating expression during illumination [15]. The synergistic effect of acetate, light, and inorganic carbon attenuates the increased expression of isocitrate lyase, the essential glyoxylate

54 cycle enzyme required for acetate assimilation [15,16]. Consistent with light-dependent metabolic
55 reprogramming, *C. reinhardtii* tends to route acetate through glyoxylate cycle–linked metabolism
56 under light, whereas in darkness mitochondrial respiration increases and TCA cycle activity
57 becomes comparatively more active [17]. An assimilatory kinetics study on heterotrophy and
58 mixotrophy in *C. reinhardtii* showed complete consumption of 20 mM acetate within the first 12
59 hours in heterotrophy. The kinetics were slower in mixotrophy, suggesting competing entry of
60 carbon via CO_2 fixation during mixotrophic growth [18]. A transcriptomic study under
61 photoautotrophic and heterotrophic conditions showed distinct gene expression patterns, with
62 genes related to glycolysis, the TCA cycle, and oxidative phosphorylation upregulated during
63 heterotrophic growth, suggesting an efficient supply of energy and carbon skeletons for rapid
64 growth of C. reinhardtii [19]. This aligns with metabolic flux balance analyses showing that C.
65 reinhardtii utilizes distinct metabolic pathways depending on its growth conditions [8]. A recent
66 isotope-assisted metabolic flux analysis indicated that acetate induces a coordinated rewiring of
67 central carbon metabolism, promoting carbon conservation via activation of the glyoxylate cycle
68 and repression of gluconeogenesis. Despite partial inhibition of photosynthesis, acetate
69 supplementation supported higher growth rates in mixotrophy compared to autotrophic growth [20].
70 Rapid metabolic adaptation to acetate may also be facilitated by post-translational protein
71 modifications, which act as a reversible switch enabling proteins to change their activities,
72 functions, or localizations in the cell [21,22].

73 *C. reinhardtii* divides by multiple fission, a mechanism in which the cell increases its size manyfold
74 (routinely more than eightfold) during a prolonged G1 phase. This growth phase is followed by
75 multiple rounds (n) of alternating S/M phases, yielding numerous daughter cells (2^n, usually 4–16).
76 This strategy allows the cells to separate growth and division both temporally and functionally [3,23].
77 During the G1 phase, the cell reaches a control point, the commitment point (CP), where it becomes

irreversibly committed to completing a division sequence even if conditions change (e.g., transfer from light to dark). The CP is conceptually similar to START in yeast and the restriction point in animal cells [3]. To reach the CP, the cell must grow until it attains a critical size. Thus, CP attainment is growth-dependent, and faster growth (at higher light and more favorable temperatures) leads to earlier CP. The critical cell size remains constant over a wide range of light conditions [24]. Prolonged growth beyond the CP leads to attainment of additional CPs; commonly, three CPs are reached within one cell cycle, resulting in the production of eight daughter cells. A mitotic sizer couples mother cell size to division number (*n*) so that daughter size distributions are uniform regardless of mother size distributions [25]. The combination of two (interlinked) sizers, a CP sizer and a mitotic sizer, ensures uniform CP and daughter cell sizes and makes these sizes an important characteristic of cell behavior.

Here, we studied cell cycle progression in synchronized cultures under different trophic conditions, reasoning that trophic conditions are a fundamental aspect of natural ecosystems and cells should be able to respond accordingly to acclimate to environmental changes. This study provides a direct comparison of the effects of the three trophic modes, under the same growth conditions, on cell growth and cell cycle progression, offering insights into optimal growth conditions and cell acclimation to changing environments. Our main goal was to analyze CP attainment under these different trophic conditions, hypothesizing that CP attainment is growth-dependent but also serves as the main ON switch for cell cycle entry, thereby translating different metabolic inputs into entry or non-entry outcomes. To this end, we sampled at biologically defined time points before and after CP attainment to identify components and mechanisms shared by or distinct to CP attainment under different trophic conditions. This study focuses on the distinct features; the common ones will be described elsewhere. The timing of the sampling points also allowed us to analyze early phases after the trophic switch. We present an integrated analysis of gene expression, cell cycle

organization, photosynthetic performance, and energy reserves in synchronized cultures grown under autotrophic (AUTO), mixotrophic (MIXO), and heterotrophic (HETERO) conditions. Of the three cultures, MIXO exhibited high metabolic activity, cellular respiration, carbohydrate and lipid metabolism, and a highly active TCA cycle. HETERO conditions showed delayed DNA replication, increased DNA damage, and elevated expression of the CDK inhibitory kinase WEE1, which was not observed in the other two conditions. The data provide comprehensive insights into the metabolic and regulatory adaptations of C. reinhardtii under varying trophic conditions and demonstrate the complex interplay between carbon availability, energy metabolism, and cell cycle progression.

Materials and methods

Growth conditions

C. *reinhardtii 21 gr* (CC–1690, wild type; Chlamydomonas Resource Center, St. Paul, Minnesota, USA, http://www.chlamy.org, accessed on 27 July 2025) was grown in tubular glass vessels (final volume 300 ml) in a high salt mineral medium (HSM) [26], at 30 ◦C, with air-CO_2 (2% v/v) aeration. The vessels were illuminated from one side by fluorescent tubes (OSRAM DULUX L55 W/950 Daylight, Milano, Italy), the light intensity at the culture vessel surface was 500 $\mu mol \cdot m^{-2} \cdot s^{-1}$ of photosynthetically active radiation (PAR).

To synchronize population growth, alternating cycles of 12 hour (h) light and 12 h dark were applied to the cultures being diluted to a constant cell number at the beginning of each light period [27,28].At the beginning of the experiment, the synchronized cell population was diluted to a starting concentration of ~1×10^6 cell. mL^{-1} in either HSM (AUTO) or TAP medium (MIXO, HETERO) [29,30] and grown at 30 °C under continuous light of 500 $\mu mol \cdot m^{-2} \cdot s^{-1}$ of PAR for AUTO and MIXO, and in dark for HETERO. All the cultures were bubbled by 2% (v/v) (2,000 ppm) CO_2 in air. The

125 experiments were run as biological triplicates, and the cultures were sampled at regular intervals
126 (either hourly or bi-hourly) (Fig. 1).

127 **Cell cycle analyses and cellular division evaluation**

128 The attainment of CPs was assessed (bi-)hourly in aliquots (1 mL) of the culture placed on HSM
129 plates and incubated in the dark at 30 °C until cell division was completed in the parental culture
130 [31]. The plates were then examined directly under a light microscope (magnification 10 × 40). For
131 each sample, the number of large single undivided mother cells and mother cells divided into 2, 4,
132 or 8 daughter cells (at least 150 mother cells) were counted, and the cumulative percentage of each
133 category was calculated and plotted against time. Mother and daughter cells can be easily
134 distinguished by differences in cell size, and cell clumps can be distinguished by the specific
135 morphology of the divided mother cells.

136 Cell division was assessed in samples that were taken (bi-)hourly, fixed with glutaraldehyde (final
137 concentration 0.2%) and observed under a light microscope (magnification 10 × 40). The
138 cumulative percentage of undivided mother cells or mother cells divided into 2, 4, or 8 daughter
139 cells were calculated and plotted against time.

140 Cell culture doubling time (*Td*) was calculated using the formula:

141 $$Td = (t_x - t_0)\ln(2) / \ln(N_x/N_0) \quad (1)$$

142 At the start of the experiment (t_0), N_0 represents the initial number of cells, while N_x denotes the
143 number of cells measured at the end of the experiment (time point t_x) [32]. The time intervals are
144 expressed in hours. Additionally, the cell division number was determined using the ratio N_x/N_0,
145 where N_0 and N_x correspond to the cell counts at the beginning and end of the experiment,
146 respectively.

147 **Cell volume and dry mass**

148 Cell volumes were measured with the Multisizer 4 (Beckman Coulter) in glutaraldehyde fixed
149 samples (final concentration 0.2%) by diluting 50 µL of fixed cells in 10 mL 0.9% NaCl. The results
150 were given as modal volume values of the cells in the sample. For determining daughter cell size,
151 10 mL aliquots from 9 h and 11 h of the cell cycle were aerated at 30 ◦C in the dark until division
152 was complete (not more than 24 h from start of illumination), samples were fixed with
153 glutaraldehyde and analyzed.

154 Biomass was separated from the medium by centrifugation of 5 mL of the cell suspension in pre-
155 weighed microtubes at 3000× g for 5 min; the sediment was dried at 105 °C for at least 12 h (until
156 stable weight) and weighed on an analytical balance (TE214S-0CE, Sartorius, Goettingen,
157 Germany) [33].

158 **Quantum yield**

159 The quantum yield of photosynthesis was measured as the F_V/F_M ratio of chlorophyll fluorescence.
160 Aliquots of 2 ml were taken from the culture and darkened for 30 min in 10 mm × 10 mm plastic
161 cuvettes at room temperature. The cell suspension was mixed gently by inverting the cuvettes
162 several times before measurement. Quantum yield was measured using an Aqua-Pen-C 100
163 (Photon Systems Instruments, Drasov, Czech Republic) set according to the manufacturer's
164 instructions [34].

165 **DNA, RNA and proteins quantification**

166 Total nucleic acids were extracted according to [35], as modified by [36]. The DNA assay was carried
167 out as described by [37], with modifications of [38]. The sediment remaining after nucleic acid

168 extraction was quantified for protein content according to the procedure described by Lowry and
169 Randall [38]. The data are expressed in pg of DNA, RNA and protein content per cell.

170 **Statistical analysis**

171 All experiments were performed in three biological replicates (n = 3). Presented results are the
172 average and standard deviations from all three replicates. MS Excel 2010 (Microsoft) with Real
173 Statistics Resource Pack (https://www.real-statistics.com/free-download/real-statistics-resource-
174 pack/, accessed on 27 May 2025) was used to generate statistics. Comparison between
175 experimental treatments was performed using the two-way ANOVA test and Tukey's HSD test. A
176 p-value < 0.05 was considered significant.

177 **RNA extraction and library preparation**

178 RNA was isolated using the ZiXpress Viral DNA/RNA Extraction Kit (Zinexts; cat. no. ZP02201-
179 192) on the ZiXpress robot (Zinexts) according to the manufacturer's instructions. Contaminating
180 DNA was removed by in-column DNase treatment (NEB; cat. no. M0303) according to the
181 manufacturer's instructions. RNA fragmentation and rRNA depletion were performed using the
182 QIAseq FastSelect kit (QIAGEN; cat. no. 334315). Libraries were prepared using the NEBNext
183 Ultra II Directional Library Prep Kit (NEB; cat. no. E7760) according to the manufacturer's
184 instructions. All purification steps were carried out using SPRIselect beads (Beckman Coulter; cat.
185 no. B23319). Library quality was assessed by agarose gel electrophoresis. The libraries were
186 subsequently sequenced by Novogene (paired end, 150 bp; PE150) on an Illumina platform.

187 **Transcriptome data analysis**

188 Raw sequencing reads were assessed for quality using FastQC [39]. Adapters were removed from and
189 the low-quality reads and cleaned using fastp [40]. Cleaned reads were mapped to indexed

190 *Chlamydomonas reinhardtii* CC-4532 v6.1 genome and transcriptome (https://phytozome-
191 next.jgi.doe.gov/) [41], using Salmon (version 1.10.2) [42]. The Salmon quantification files were made
192 readable using tximport [39]. PCA of the transcriptome was performed separately on each comparison
193 using the R package PCA tools (v2.16.0) on mRNAs with a minimum average FPKM (17, 369
194 genes). The count data were tested for differential expressions using edgeR (v4.8.2) [43], with the
195 GLM likelihood algorithm [44]. Significant differential expression was defined as |log2 fold-
196 change | > 2, FDR < 0.05. Mean transcript abundances (as FPKMs) were Z-score normalized across
197 different trophic conditions (AUTO VS MIXO, HETERO vs AUTO, HETERO vs MIXO).
198 Heatmaps were generated using the R package pheatmap (version 1.0.13. https://CRAN.R-
199 project.org/package=pheatmap). Functional enrichment analysis was performed using MapMan [45]
200 annotations for *Chlamydomonas reinhardtii* using *Chlamydomonas reinhardtii* CC-4532 v6.1.
201 Common transcriptional expression patterns throughout AUTO, MIXO, and HETERO treatments,
202 we performed by k-means clustering of their normalized expression patterns, implemented by
203 pRocessomics R package (v.0.1.13, github.com/Valledor/pRocessomics)[46].

204 Results

205 Growth in heterotrophy is very slow

206 To directly compare the effect to the different trophic regimes on cell growth, metabolism, and cell
207 cycle progression, we synchronized cultures of *C. reinhardtii* in minimal medium and exposed
208 them to different trophic regimes for a duration of a single cell cycle (Fig. 1). The experiment
209 started with cultures composed of daughter cells at concentration approximately $1*10^6$ cell.mL^{-1}.
210 The individual cultures were provided with CO_2 alone (AUTO) or in combination with acetate
211 (MIXO, HETERO) in light (500 µmol m^{-2} s^{-1}, AUTO, MIXO) or in dark (HETERO). Cellular
212 growth in algae is largely governed by the activity of organelles such as chloroplasts containing

213 photosynthetic machinery. Chlorophyll *a* fluorescence is a quick and reliable indicator for
214 detecting stress to photosynthesis responses in microalgae and serves as physiological indicator of
215 cellular responses to varying environmental conditions [47]. To assess the efficiency of light energy
216 conversion during photosynthesis, we measured the maximum quantum yield of photosystem II
217 (Fv/Fm). All the values were within the normal physiological range, confirming no damaging effect
218 of any trophic regime nor the light intensity used (Fig. 2c). AUTO and MIXO depicted similar
219 patterns of PSII (Fv/Fm) with slight drop at 1 hour after the light onset, then improved to previous
220 values. At the end of cultivation, the QY for the MIXO culture dropped slightly, but for all
221 conditions it remained above ~0.5 suggesting non-stress growth conditions and healthy
222 photosynthetic machinery [48]. Between the two light grown cultures there was no difference in
223 chlorophyl accumulation, while the dark grown HETERO culture did not accumulate any further
224 chlorophyl (Fig. 2h, i).

225 When assessing the growth, the MIXO cultures grew the fastest of the three (Fig. 2a). This was
226 further confirmed by final dry cell weight (DCW) which was highest under MIXO, reaching 617.07
227 ± 130.79 $pg \cdot cell^{-1}$, followed by AUTO at 308.85 ± 63.85 $pg \cdot cell^{-1}$. HETERO cultures grew the
228 slowest and accumulated the lowest biomass, 44.72 ± 14.08 $pg \cdot cell^{-1}$ (Fig. 2a). The cell volumes
229 (μm^3), another growth parameter, ranged in AUTO between 56.73 μm^3 ± 1.00 (in young daughter
230 cells at the beginning of the cell cycle) and 329.17 μm^3 ± 41.39 (mature mother cells at the 12th h
231 before division), i.e. increase about 5.8 fold (Fig. 2b). These large cells began dividing after 14 h,
232 resulting in a decrease in cell volume to 56.73 μm^3 ± 2.07 and a concomitant increase in cell density.
233 Similarly, in MIXO cell volumes ranged from 49.56 μm^3 ± 5.49 in young daughter cells to 368.23
234 μm^3 ± 49.01 in mature mother cells at the 14th h, i. e. increase about 7.4 fold. In HETERO, cell
235 volumes didn't change significantly, young daughter cells of size 52.04 μm^3 ± 1.99, remained same
236 in size throughout experiment (Fig. 2b). Total RNA content increase (5.7-fold in MIXO, 10-fold in

237 AUTO) did not match the extent of cell volume increases, suggesting different cell composition
238 between the two growth modes (Fig. 2e). In HETERO cultures, the accumulation of total RNA was
239 notably slow, and the RNA content increased only ~1.49-fold (Fig. 2e). Similar pattern was also
240 seen for the bulk protein content (Fig. 2f).

241 Starch accumulation was the highest in MIXO conditions, increasing more than 43-fold over a
242 period of 20 hours. In AUTO, starch content increased about 33-fold within 19 hours. The lowest
243 starch accumulation was observed in HETERO, with increase l.7-fold, i. e. less than two-fold
244 effectively decreasing the cell starch content between the daughter cells at the beginning and end
245 of the experiment (Fig. 2g). Lipid accumulation was also notably higher in MIXO,
246 reaching 13.32 $pg \cdot cell^{-1}$ within 20 hours. In comparison, AUTO exhibited lipid levels
247 approximately ten times lower, with a maximum of 2.16 $pg \cdot cell^{-1}$ over the same time frame. In
248 HETERO, the lipid content was negligible at the threshold of detection, and no lipid accumulation
249 was observed throughout the growth period (Fig. 2j).

250 **Cell Cycle Progression Differs between Growth Regimes**

251 Synchronized culture in AUTO, sequentially attained three CPs, with midpoints at approximately
252 3, 6, and 12 h after the onset of light (Fig. 3a). The total cell cycle duration in AUTO was 19 hours.
253 Similarly, MIXO attained three CPs, with midpoints at approximately 2, 4, and 10 h (Fig. 3b). The
254 CP attainments in MIXO were advanced compared to AUTO. In HETERO, CP attainment was
255 delayed with only about 50 % of the cells committing. The committed cells passed two CPs with
256 midpoints at approximately 20 and 24 h (Fig. 3c). Consistent with the low commitment rate, only
257 ~50% of cells divided, most producing four daughter cells (division number = 2). The critical sizes
258 at which first CP was attained were (Table 2).

259 S/M phase started by the 11th to 12th hour of the cell cycle in both AUTO and MIXO. It was
260 completed by the 16th hour in AUTO and 20th hour in MIXO. During this time, DNA multiplied
261 about 10-times both in AUTO (from 0.2 pg. cell^{-1} to 2.36 pg. cell^{-1}) and MIXO (from 0.39 pg. cell^{-}
262 ^{1} to 4.13 pg. cell^{-1}) (Fig. 2d) corresponding to the production of at least 8 daughters per mother
263 cells. In HETERO, the total DNA rose about 4-fold (from 0.11 pg·cell^{-1} to 0.52 pg·cell^{-1}) over the
264 60-hour cultivation period (Fig. 2d).

265 **Distinct transcriptomic profile in heterotrophy**

266 Due to differences in growth among the regimes, sampling them at the same time after the trophic
267 switch would introduce additional variability, as samples would be affected by both the trophic
268 regime and the growth rate. To avoid this, we sampled for transcriptomics at biologically equivalent
269 timepoints: right before CP attainment (Pre-CP) and soon after CP attainment (Post-CP), that is, at
270 times when cells in any condition reached critical size and were ready to enter the cell cycle (Fig.
271 1). The timing of Pre-CP and Post-CP sampling was determined independently for each trophic
272 condition based on the commitment point assay, ensuring that samples corresponded to similar
273 biological states despite differences in growth rates between AUTO, MIXO, and HETERO. While
274 CP attainment in AUTO and MIXO conditions occurred at a similar timepoint early after cell cycle
275 start, it was significantly delayed in HETERO cultures. As a result, the samples from AUTO and
276 MIXO conditions were inherently closer both in biologically and temporally. Given the rapid CP
277 attainment in AUTO and MIXO, these samples reflected the immediate effects of the trophic switch.
278 In contrast, samples from HETERO cultures reflected acclimation to the trophic switch. The
279 sampling design thus captured (i) transcriptional responses associated with early metabolic
280 reprogramming after the trophic switch (Pre-CP), and (ii) entry into cell division (Post-CP).

281 We detected approximately 17,369 genome-wide transcripts in all trophic regimes (AUTO, MIXO,
282 and HETERO). Across the genome, RNA abundances varied depending on the trophic conditions.
283 Principal component analysis (PCA) of the RNA-Seq data revealed that most transcriptomic
284 variation was driven by differences in growth conditions, with only a smaller proportion
285 attributable to the cell cycle stage (Fig. 4). Additionally, strong similarity was found between
286 biological replicates, as demonstrated by Pearson correlation coefficients (*r*), confirming
287 reproducibility (Supplementary Figure 1 and Supplementary Data Set 1).

288 We employed differential expression modeling to identify differentially expressed genes (DEGs)
289 that were either overlapping or uniquely upregulated or downregulated in AUTO, MIXO, and
290 HETERO treatments (Supplementary DataSet_2, 3, and 4). Differentially expressed genes were
291 considered significant if they had an adjusted p-value ≤ 0.05 and an absolute log2 fold change
292 ($|\log2FC|$) ≥ 2. The largest number of significant DEGs was identified between Post-CP MIXO vs.
293 Post-CP HETERO, with approximately 6,098 significantly altered transcripts—3,328 upregulated
294 and 2,770 downregulated (Fig. 5f; Supplementary DataSet_4). This was followed by Post-CP
295 AUTO vs. Post-CP HETERO, with about 5,017 significant transcripts, of which 2,455 were
296 upregulated and 2,562 were downregulated (Fig. 5e; Supplementary DataSet_3). The difference
297 between mixotrophic to heterotrophic growth and switch from autotrophic to heterotrophic growth
298 was marked by strong oscillation in the expression of genes involved in heterotrophic metabolism,
299 indicating that the absence of light and the presence of external carbon sources strongly induced
300 heterotrophic metabolism. Furthermore, in Post-CP MIXO vs. Post-CP AUTO, approximately
301 4,575 significant DEGs were observed, with 2,079 upregulated and 1,196 downregulated (Fig. 5d;
302 Supplementary DataSet_2). Additional shared and unique responses in these comparisons were
303 also identified (Supplementary DataSet_2). To further analyze the biological processes underlying
304 the global expression shifts, we performed pathway-level analyses. Below we outline several

305 examples of metabolic pathways with distinct behavior under different trophic conditions.
306 Differential expression was evaluated using log2 fold-change > 2 and FDR < 0.05, and expression
307 patterns were also assessed by Z-score normalization.

308 ***Photosynthesis***

309 In Post-CP MIXO compared with Post-CP AUTO, photosynthesis-related genes were upregulated,
310 including the PSI light-harvesting protein LHCA4 (logFC = 2.19), LHCII chlorophyll a/b–binding
311 proteins such as LHCBM1 (logFC = 3.19), and LHCII antenna subunits (logFC = 3.17)
312 (Supplementary DataSet_2). In Post-CP HETERO compared with Post-CP AUTO, we found
313 similar patterns, with LHCA4 (logFC = 3.43) and LHCA1 (logFC = 2.22874) upregulated in Post-
314 CP HETERO (Supplementary DataSet_3). [49] demonstrated that acetate in TAP medium protects *C.*
315 *reinhardtii* from photoinhibition by altering the PSII charge recombination reaction, thus lowering
316 the production of singlet oxygen ($^1O_2$) compared to autotrophy. In contrast, it has also been reported
317 that under light conditions, acetate suppresses the light-induced increase in LHCII chlorophyll *a/b*–
318 binding proteins from approximately 6 hours onward. Despite the difference in timing, our results
319 may be consistent with this phenomenon as the growth conditions used in our experiments were
320 supporting faster growth. Alternatively, we captured the initial induction phase rather than the later
321 acetate-mediated repression [15]. In line with this, recent isotope-assisted metabolic flux analyses
322 have shown that acetate decreases $^{13}CO_2$ assimilation and Calvin-Benson-Bassham (CBB) cycle
323 flux by approximately 31%, thereby partially suppressing photosynthesis. Despite this reduction,
324 mixotrophic cells exhibit higher growth rates than autotrophic cells. These findings suggest that
325 cells strategically downscale photosynthetic activity to reduce biosynthetic and energetic costs
326 when acetate provides an efficient external carbon source [20].

327 Cytochrome b6/f complex genes (petD and petG) showed an increased trend in Post-CP MIXO
328 based on z-score normalization and were downregulated in Post-CP HETERO (Fig. 4), indicating
329 trophic state-specific remodeling of PSI light harvesting and the electron transport chain.
330 Interestingly, we also found that, in Post-CP HETERO vs. Post-CP MIXO, the FdC-type ferredoxin
331 electron carriers (FdC2 and Fd1/2/3) were upregulated in Post-CP MIXO; increased ferredoxin-
332 dependent electron partitioning may support light-driven metabolism and biosynthetic demands
333 during the post-CP-commitment phase in MIXO, as Fd completes the linear electron transport
334 chain generating NADPH via ferredoxin–$NADP^+$ reductase. In addition, upregulation of the
335 thylakoid grana stacking regulatory factor (CRUT) was also found in Post-CP MIXO compared to
336 Post-CP HETERO.

337 ***Acetate assimilation***

338 In the Post-CP MIXO vs. Post-CP AUTO comparison, the acetate transporter *GFY1-5* (logFC =
339 2.91), acetyl-CoA synthase (*ACS1*) (logFC = 2.01), and phosphotransacetylase/phosphate
340 acetyltransferase (*PAT*) (logFC = 2.02) were significantly upregulated (Fig. 5e), indicating
341 enhanced acetate uptake and increased channeling of acetate-derived carbon into the acetyl-CoA
342 pool and downstream central metabolism in mixotrophic cells. The involvement of GFY membrane
343 proteins in acetate uptake has been demonstrated in *Escherichia coli* [50], *Citrobacter koseri* [51],
344 *Saccharomyces cerevisiae* [52], and *Aspergillus nidulans* [53], as well as their structural homology with
345 *CrGFY1-5* [54]. In addition, *GFY5* was strongly regulated in Post-CP HETERO relative to Post-CP
346 AUTO (logFC = 4.86), consistent with the concomitant induction of *ACS2* (logFC = 3.04), a
347 gateway enzyme that converts acetate to acetyl-CoA for entry into the glyoxylate cycle/TCA cycle
348 and downstream central carbon metabolism [55]. Strikingly, when we compared Post-CP MIXO vs.
349 Post-CP HETERO, *GFY4* (logFC = 6.20) was upregulated in Post-CP HETERO. This was also

350 evident in the Z-score trend, with upregulation of *ACS* and *GFY1–5*, signifying enhanced acetate
351 uptake and increased conversion of acetate into the acetyl-CoA pool to support carbon and energy
352 metabolism during heterotrophic growth.

353 ***Photorespiration and carbon capture***

354 Among the photorespiration-associated genes, serine glyoxylate aminotransferase (*SGA1*) was
355 upregulated (logFC = 2.21) in Post-CP MIXO compared to Post-CP AUTO (Fig. 5d;
356 Supplementary DataSet_2). Z-score trends showed coordinated upregulation of core
357 photorespiratory components, including *AGT1*, *SHMT1*, *HPR1*, and the terminal enzyme *GLYK1*,
358 consistent with increased photorespiratory recycling of 2-phosphoglycolate/glycolate to 3-
359 phosphoglycerate to support redox homeostasis and carbon flux during mixotrophic growth (Fig.
360 6). A similar induction pattern was observed in Post-CP HETERO compared to Post-CP AUTO.
361 Notably, although both conditions used acetate, the Post-CP MIXO vs Post-CP HETERO
362 comparison showed higher Z-scores for *AGT1*, *SHMT1*, *HPR1*, and *GLYK1* in MIXO, indicating
363 higher photorespiratory activity in MIXO than in HETERO (Fig. 5f).

364 Genes involved in carbon capture and fixation were upregulated in Post-CP MIXO compared to
365 Post-CP AUTO, including key CBB cycle components such as fructose-bisphosphate aldolase
366 (*FBA2–3*), glyceraldehyde-3-phosphate dehydrogenase (*GAPA1*), sedoheptulose-1,7-
367 bisphosphatase (*SBP1*), and transketolase (*TRK1*) (Fig. 6). In parallel, genes involved in central
368 carbohydrate metabolism also showed higher expression, including the glycolytic genes enolase
369 (*ENO1*), phosphofructokinase (*PFK1*), fructose-1,6-bisphosphate aldolase (*FBA3*), and pyruvate
370 kinase (*PYK1*), consistent with elevated carbon flux to support post-CP commitment energy and
371 biosynthetic demands under mixotrophic growth. In contrast, these genes were expressed at lower
372 levels in Post-CP HETERO compared to both Post-CP MIXO and Post-CP AUTO, indicating that

373 Post-CP MIXO maintains more photosynthetically driven, carbon assimilatory metabolic flux than
374 Post-CP AUTO and Post-CP HETERO, despite the availability of acetate as an external carbon
375 source. Furthermore, we observed repression of gluconeogenesis-associated genes in Post-CP
376 MIXO compared to Post-CP AUTO; Post-CP HETERO showed a similar trend, including
377 downregulation of pyruvate phosphate dikinase (*PPD1*). However, pyruvate carboxylase 1 (*PYC1*)
378 was upregulated in Post-CP MIXO compared to both Post-CP HETERO and Post-CP AUTO. When
379 acetyl-CoA is abundant, pyruvate carboxylase diverts pyruvate away from the TCA cycle,
380 redirecting carbon toward different metabolic routes [56].

381 ***Oxidative pentose phosphate pathway***

382 Significant upregulation of Glucose-6-phosphate-1-dehydrogenase (*GLD1*) (logFC = 2.31) was
383 found in Post-CP MIXO compared to Post-CP AUTO. Higher *GLD1* expression has been
384 associated with increased oxidative pentose phosphate pathway (OPPP)–driven NADPH
385 production, aligning with acetate-supported metabolism, biosynthetic demand, and/or redox
386 balancing when carbon metabolism is elevated and/or photosynthetic reductant is constrained [57].
387 Consistently, Z-score analysis revealed increased expression of multiple OPPP-associated genes in
388 Post-CP MIXO, including *GLD1*, 6-phosphogluconolactonase (*PGL1*), ribose-5-phosphate
389 isomerase (*RPI1*), transketolase (*TRK1*), and ribulose-phosphate 3-epimerase (*RPE2*). In contrast,
390 *GLD1* was significantly upregulated (logFC = 2.29) in Post-CP AUTO compared to Post-CP
391 HETERO (Supplementary DataSet_3), indicating reduced OPPP participation under heterotrophic
392 post-CP commitment conditions relative to autotrophy and mixotrophy.

393 ***Glyoxylate and TCA pathway***

394 Two key glyoxylate cycle genes, isocitrate lyase (*ICL1*) (logFC = 4.23) and malate synthase
395 (*MAS1*) (logFC = 5.74), were significantly upregulated in Post-CP MIXO relative to Post-CP

396 AUTO (Fig. 5d). Their induction was even more pronounced in Post-CP HETERO vs. Post-CP
397 AUTO, reaching logFC values of 9.15 *(ICL1*) and 7.46 (*MAS1*), respectively (Fig. 5e). In addition,
398 Z-score analysis showed higher expression of *ICL1* and *MAS1* in Post-CP HETERO compared to
399 Post-CP MIXO, signifying higher glyoxylate activity in HETERO than in MIXO (Fig. 6).

400 Additionally, multiple TCA cycle genes – citrate synthase (*CIS2*), isocitrate dehydrogenase (*IDH2*),
401 2-oxoglutarate dehydrogenase (*OGD1*), succinyl-CoA ligase (*SCLA1*), fumarate hydratase
402 (*FUM2*), and malate dehydrogenase (*MDH4*)—showed higher expression in Post-CP MIXO than
403 in Post-CP HETERO. Notably, the succinate dehydrogenase assembly factor *SDHAF4* (logFC =
404 4.13) and *SCLA1* (logFC = 2.02) were strongly upregulated, supporting a more active TCA-linked
405 respiratory metabolism under mixotrophic growth (Fig. 6).

406 ***Amino acid metabolism and redox homeostasis***

407 Ornithine transaminase (*OTA1*; logFC = 2.40) and glycerol-3-phosphate dehydrogenase (*GPD2*;
408 logFC = 2.92) were significantly upregulated in Post-CP MIXO compared with Post-CP AUTO
409 (Fig. 5e). Z-score profiling further showed enrichment of aspartate aminotransferase (*AST2*),
410 proline dehydrogenase (*PDY1-2*), and threonine dehydratase (*THD1*). In line with this, several
411 genes linked to branched-chain amino acid degradation were also elevated in Post-CP MIXO,
412 including 3-hydroxyisobutyrate dehydrogenase (*HID1*), aldehyde dehydrogenase (*ALDH6*), and
413 thiosulfate sulfurtransferase (*TSU1*), relative to Post-CP AUTO. Taken together, the depletion of
414 branched-chain amino acids and proline supports enhanced amino acid catabolism and a
415 concomitant rerouting of central carbon fluxes under MIXO. Proline catabolism is consistent with
416 previous studies reporting upregulation of *PDY1–2*, indicating that proline oxidation can contribute
417 to ATP production during nutrient remobilization in *Arabidopsis thaliana* [58]. Likewise,
418 acetylornithine deacetylase (*AOD1*; logFC = 2.85), ornithine aminotransferase (*OAT1*; logFC =

419 2.56), glutamate 5-kinase (*PROBI*; logFC = 2.49), and glycerol-3-phosphate dehydrogenase
420 (GPD2; logFC = 2.83) were upregulated in Post-CP MIXO compared with Post-CP HETERO
421 (Supplementary DataSet_5).

422 ***Effect of trophic regime on cell cycle regulation***

423 In both AUTO and MIXO, *CDKA1* expression was relatively low in Pre-CP and increased in Post-
424 CP (Fig. 7). The Z-score showed stronger *CDKA*1 upregulation in Post-CP MIXO than in Post-CP
425 AUTO. *CDKB1* increased from Pre-CP to Post-CP in AUTO, but in MIXO it showed the opposite
426 pattern, being reduced in Post-CP and relatively higher at Pre-CP. *CDKB1* expression has been
427 associated first with pre-commitment and, second, much more strongly during the S/M phase [2,59-
428 61]. Similar mitosis-associated upregulation has also been described for other CDKB-family
429 members in plants [62,63]. *CDKC1* showed a similar pattern in both AUTO and MIXO, with lower
430 expression at Pre-CP and higher expression at Post-CP (Fig. 6). *CDKC1* levels were consistently
431 higher in MIXO than in AUTO at both Pre-CP and Post-CP. In contrast, *CDKD1* showed higher
432 expression at Pre-CP than at Post-CP in both AUTO and MIXO, with overall expression again
433 being higher under MIXO. *CYCA1* and *CYCB1* displayed patterns similar to *CDKB1*. The
434 expression of *E2F1–DP1* and the retinoblastoma protein (*MAT3*) was higher at Post-CP than at
435 Pre-CP under both AUTO and MIXO conditions; at the Post-CP stage, their expression was higher
436 in MIXO than in AUTO [64].

437 DNA polymerases *POLA2/4* and *PODA1/2* and the ribonucleoside-diphosphate reductase large and
438 small subunits (*RIR1–2*) showed higher expression at Pre-CP compared to Post-CP in both AUTO
439 and MIXO. The *POLA2/4* and *PODA1/2* Pre-CP expression was higher in MIXO than in AUTO.
440 Replication factor C subunits (*RFC1–5*) were strongly upregulated in Post-CP MIXO, together
441 with increased expression of *MCM5–7*, whereas these DNA replication genes were downregulated

442 in Post-CP AUTO, indicating active replication machinery in Post-CP MIXO (Fig. 6,
443 Supplementary DataSet_5).

444 When comparing MIXO and HETERO, *CDKA1* showed an increased expression trend from PreCP
445 to Post-CP under both conditions; both PreCP and Post-CP expression levels were markedly higher
446 in HETERO than in MIXO (Fig. 6). This is consistent with reports showing that CDKA1 protein
447 is present throughout the cell cycle, whereas substantial CDKA1-associated kinase activity is
448 detected primarily in actively dividing *C. reinhardtii* [65]. *CDKB1* showed higher expression in Pre-
449 CP MIXO and was downregulated at Post-CP MIXO, whereas the opposite trend was observed in
450 HETERO, with lower expression at Pre-CP and increased expression at Post-CP. CDKB1 is
451 associated first with pre-commitment and is most strongly induced during S/M [2,59-61]. *CYCA1* and
452 *CYCB1* showed higher expression at Post-CP in HETERO compared to MIXO.

453 Transcripts corresponding to the E2F1–DP1 regulatory module and the MAT3/RB complex were
454 more abundant in Post-CP HETERO than in Post-CP MIXO. Consistently, Post-CP HETERO also
455 exhibited markedly higher expression of core cell cycle and DNA replication machinery, including
456 *APC1–10*, *MCM2–7*, and *RFC1–5*, relative to Post-CP MIXO. In addition, Post-CP HETERO
457 showed elevated expression of genes implicated in DNA damage tolerance and repair, including
458 DNA polymerase η (*POLH2*), DNA polymerase ι (*POLI1*), DNA polymerase ζ (*POLZ1*), and the
459 structure-specific endonuclease *XPF1* (Fig. 6, Supplementary DataSet_5). Likewise, higher
460 expression of *WEE1* was found in Post-CP HETERO than in Post-CP MIXO. Wee1 kinase is
461 regarded as a mitotic inhibitor and acts as a checkpoint for DNA damage response. In *Arabidopsis*
462 *thaliana*, elevated *WEE1* kinase expression suppressed growth by arresting cells in the G_2 phase of
463 the cell cycle, acting as part of the DNA integrity checkpoint that couples mitosis to DNA repair in
464 cells that suffer DNA damage [66].

465 # Discussion

466 ## Growth and photosynthesis

467 Acetate supplementation is known to enhance metabolism and accelerate growth in many green
468 algae [10,67,68]. Similarly, there was greater accumulation of total lipid and starch in MIXO compared
469 to AUTO and HETERO (Fig. 2h, k). This aligns with metabolite studies showing higher
470 accumulation of both starch and triacylglycerol (TAG) in mixotrophy compared to heterotrophy [69].
471 This mechanism appears to be general for other algae, such as Parachlorella kessleri TY [70]. Light
472 harvesting efficiency is influenced by both the composition and concentration of photosynthetic
473 pigments. Pigment concentration depends on biomass density and growth conditions, while
474 composition is primarily affected by the intensity and quality of light [71]. Among all treatments,
475 AUTO showed the highest total chlorophyll content, accompanied by high Fv/Fm. A higher Fv/Fm
476 ratio is commonly regarded as increased photosynthetic efficacy, whereas a lower ratio implies
477 PSII photoinhibition [72]. The lowest chlorophyll content was found in HETERO; however, Fv/Fm
478 remained stable. This is consistent with other algae, where total chlorophyll moderately decreases
479 under mixotrophic conditions and is severely reduced in heterotrophy [73].

480 Based on the transcriptomics, photosynthetic traits were not significantly affected in MIXO
481 compared to AUTO. However, antenna subunits (LHCA4, LHCBM1, LHCII) and cytochrome b6/f
482 complex genes (petD and petG) were upregulated in Post-CP MIXO. In contrast, the RuBisCO
483 large subunit (rbcL) decreased slightly in MIXO, consistent with the established effect of acetate
484 minimizing biosynthetic and energetic investment when an efficient external carbon source is
485 available [17,20,74]. Together, these data suggest that MIXO cells maintain photochemical electron
486 transport [75] while selectively reducing investment in carbon fixation machinery, consistent with
487 acetate partially substituting for carbon derived from the CBB cycle (see below). Acetate-derived

488 carbon can substitute for half the photoautotrophically generated biomass, while photosynthesis
489 provides ATP and reductant for acetate assimilation [76]. In heterotrophy, the expression of the PSI
490 light-harvesting component (LHCA4), the PSII core reaction-center genes (psbA (D1) and psbD
491 (D2)), and the RuBisCO subunits (rbcL, RBCS1, and RBCS2) increased, consistent with
492 observations in other green algae [77,78]. This suggests that PSI/PSII and carbon-fixation machinery
493 are maintained under heterotrophy, rather than being fully unused (Fig. 6). Whether this reflects
494 functional maintenance or transcriptional persistence without corresponding activity is yet to be
495 determined, but Fv/Fm ratios suggest that PSII is potentially functional.

496 **Acetate assimilation**

497 Mixotrophy reorganizes central carbon metabolism to optimize carbon retention, redox balance,
498 and biosynthetic fluxes. Acetate assimilation, or acetyl-CoA ligation, occurs to varying extents in
499 all three intracellular compartments: 1) via a cytosolic citrate synthase followed by transport into
500 mitochondria for the TCA cycle, 2) by direct uptake into mitochondria, conversion through a
501 mitochondrial citrate synthase, and processing through the TCA cycle, and 3) by direct assimilation
502 into fatty acids in the plastid [79]. Furthermore, acetate assimilation is associated with an increased
503 number of peroxisomes and elevated expression of genes encoding putative glyoxysomal proteins
504 [80]. In our experiments under MIXO, both transcripts linked to acetate assimilation (GFY1–5, ACS1,
505 PAT) and to glyoxylate shunt genes (ICL1, MSA1) were upregulated. However, these genes were
506 expressed even more strongly in Post-CP HETERO, indicating that acetate assimilation and
507 glyoxylate cycle flux were more active in HETERO than in MIXO. This is consistent with the
508 central role of the glyoxylate cycle in acetate assimilation in both HETERO and MIXO [81]. In
509 addition to the glyoxylate cycle, the TCA cycle remains active under mixotrophy, with acetate-
510 derived carbon rerouted through the glyoxylate shunt to produce succinate and malate while

511 bypassing TCA decarboxylation steps and conserving carbon [20]. Consistent with this, nearly all
512 TCA cycle transcripts were upregulated in Post-CP MIXO compared to Post-CP AUTO and Post-
513 CP HETERO (Fig. 8).

514 During mixotrophy in the green alga Chlorella sorokiniana, light enhances photorespiration to
515 accelerate the glyoxylate cycle and release acetate-derived CO_2 for the CBB cycle [82]. Specifically,
516 photorespiration produces glyoxylate, which, in the glyoxylate cycle, condenses with acetyl-CoA
517 to form malate, effectively linking photorespiration with acetate assimilation. Glyoxylate can be
518 converted into glycine, releasing CO_2 from acetate, followed by carbon fixation in the CBB cycle.
519 A similar mechanism may also occur in C. reinhardtii, as transcripts associated with
520 photorespiration – glycolate transporter (PLGG1), glycine decarboxylase complex (GCST1), and
521 serine hydroxymethyltransferase (SHMT1)—were upregulated in Post-CP MIXO (Fig. 8). The
522 upregulation of GCST1 and SHMT1 indicates that glycine is transported into the mitochondria,
523 where two glycine molecules undergo deamination and decarboxylation by GCST1 and SHMT1,
524 resulting in the formation of one molecule each of serine, ammonia, and carbon dioxide [83]. In
525 HETERO, these transcripts were also upregulated, with abundance exceeding AUTO but remaining
526 below MIXO, consistent with photorespiration being maintained in heterotrophy but operating at
527 a reduced level compared with mixotrophy. In line with this, several CBB transcripts (RuBisCO
528 subunits rbcL, RBCS1, RBCS2, fructose-1,6-bisphosphate aldolase (FBA), NADPH-dependent
529 malate dehydrogenase (NADP-MDH)) were elevated in HETERO, suggesting continued CO_2
530 fixation, with a contribution from internally released CO_2 from acetate catabolism. Flux balance
531 analysis suggested that mixotrophy also activates the oxidative pentose phosphate (OPP) pathway
532 [84], which functions as a carbon sink, redirecting photosynthate toward nucleotide biosynthesis and
533 thereby supporting increased growth rate and biomass production under mixotrophy. In this way,
534 mixotrophy supports mitochondrial respiration while reducing carbon-fixation flux and NADPH

535 demand [84]. In our experiments, OPP pathway intermediates were most strongly upregulated in Post-
536 CP MIXO, showed a more modest increase in Post-CP AUTO, and were downregulated in Post-
537 CP HETERO (Fig. 8). The downregulation in HETERO may be consistent with an inactive OPP
538 pathway in heterotrophy in another green alga, Chlorella vulgaris [85]. Taken together, the
539 transcriptional profile supports coordinated metabolic rewiring under mixotrophy, in which acetate
540 assimilation, glyoxylate shunt activation, increased TCA flux, and elevated photorespiration
541 collectively promote carbon conservation and redox flexibility. Rather than representing parallel
542 pathways, these modules appear functionally integrated to maximize biomass production while
543 minimizing carbon loss.

544 **Stress response**

545 The strong transcriptional induction of stress-associated genes in HETERO likely reflects the
546 metabolic imbalance resulting from reliance on acetate without photosynthetic energy input. The
547 HETERO conditions rapidly induce transcripts that encode heat shock proteins (HSPs, HSP70),
548 the ribosome-associated molecular co-chaperone (ZRF1), and reactive oxygen species (ROS)
549 scavenging genes, including superoxide dismutases (FSD1, MSD1), glutathione peroxidases
550 (GPX1/2/++), catalases (CAT1/2/3), and gamma-tocopherol methyltransferase (VTE4). HSP70
551 genes are naturally induced by a dark-to-light shift in C. reinhardtii [86,87] and are regulated by a
552 circadian rhythm to prepare cells for subsequent exposure to high light [88,89]. The HSPs (HSP90,
553 HSP110, mitochondrial HSP70), genes involved in superoxide dismutase activity, glutathione- and
554 thiol-based redox regulation, and tocopherol biosynthesis were also upregulated in MIXO,
555 suggesting that, rather than indicating stress, this expression is related to metabolic reprogramming.
556 This upregulation of HSP70 seems to be a general mechanism as it was shown also in
557 mixotrophically grown Chlorella vulgaris [90]. Thus, HSP70 induction may reflect primarily

558 remodeling demands, such as rebalancing light-harvesting complexes, PSII repair, thylakoid
559 protein turnover, and changes in ROS production during trophic transition or possible proteostatic
560 stress.

561 **Cell cycle in different trophic regimes**

562 The original hypothesis driving this study was to identify common and distinct transcriptional
563 patterns between the trophic regimes. While the common features will be described elsewhere, here
564 we focus on differences among the treatments. Comparing Post-CP MIXO with Post-CP AUTO
565 showed similar patterns of cell cycle gene expression with generally higher expression in MIXO
566 conditions (Fig. 7). We were able to confirm the established patterns [59] of CDKB1, CYCA1, and
567 CYCB1 with increase in Pre-CP MIXO and decreasing in Post-CP MIXO. Because our sampling
568 was around the CP, we were unable to observe the major upregulation of these genes during the
569 S/M phase [2,59,60]. In contrast, the Post-CP HETERO showed increased expression of most cell cycle
570 genes, including those involved in DNA replication, DNA replication initiation factors, the MCM
571 complex, CDKs, ribonucleosides, and plastid division (Fig. 7). The CDK-inhibitory kinase WEE1
572 was highly expressed in Post-CP HETERO, along with several DNA repair factors, including DNA
573 repair glycosylase (AGE3), uracil DNA glycosylase (UNG1), and translesion DNA polymerases η,
574 ι, ζ, and κ. Similarly, leucine zipper (bZIP) and WRKY family transcription factors were also
575 upregulated in Post-CP HETERO. Both families are associated with stress-responsive regulation,
576 with bZIPs reported in oxidative stress tolerance in C. reinhardtii [91,92] and WRKYs widely reported
577 in plant stress responses [90,93,94]. A simple explanation stems from very slow growth and late CP
578 attainment in HETERO, which is reflected in the sampling. For both AUTO and MIXO, the Post-
579 CP samples were collected early in the cell cycle and at least six hours before the onset of S/M
580 phase. In contrast, in HETERO, the Post-CP sample preceded the onset of S/M phase by only 2–3

581 hours. Therefore, it is plausible that the established upregulation of cell cycle genes, known to
582 occur before S/M onset, had already begun in the Post-CP HETERO samples. Given that WEE1
583 transcription increases prior to S/M entry, its elevated expression in HETERO is consistent with a
584 later sampling window closer to mitotic onset [60] rather than a stress-induced checkpoint activation.
585 Alternatively, it remains possible that genes encoding proteins involved in cell division, especially
586 CDKs, DNA replication, and mitotic entry, were abnormally and overwhelmingly more highly
587 expressed in Post-CP CP HETERO compared to Post-CP CP MIXO and Post-CP CP AUTO. This
588 correlates with the commitment point analysis (Fig. ---), which showed that fewer cells reached the
589 commitment point in HETERO and that cell-cycle progression was delayed compared with the
590 other conditions. This would be consistent with observations in the C. reinhardtii cht7 mutant
591 grown under nitrogen-depleted conditions, which also shows higher expression of cell-cycle genes
592 with ≥2C DNA and reduced growth, indicating premature or unscheduled DNA replication
593 compared to wild type [95,96].

594 Collectively, these findings suggest that trophic regime affects not only metabolic flux distribution
595 but also redox balance, proteostasis, and the timing of cell-cycle transitions. Our results indicate
596 that autotrophic, mixotrophic, and heterotrophic growth in Chlamydomonas are associated with
597 distinct transcriptional adjustments that coordinate central carbon metabolism, photosynthetic
598 capacity, and cell-cycle progression. Mixotrophy does not appear to represent a simple additive
599 coexistence of autotrophic and heterotrophic programs; instead, it involves coordinated metabolic
600 adjustments linked to altered carbon fixation investment and cell-cycle progression. In contrast,
601 heterotrophy weakens the connection between metabolic input and cell-cycle timing, resulting in
602 delayed commitment and stress-associated transcriptional signatures. These findings provide a
603 framework for understanding how carbon availability influences metabolic organization and cell-
604 cycle regulation in photosynthetic eukaryotes.

Funding

This research was funded by the Grant Agency of the Czech Republic, grant no. 22-21450S, and by Institutional Research Concept no. AVOZ61388971.

Acknowledgements

We are obliged to the technical staff of the Laboratory of Cell Cycles of Algae for excellent technical support.

References

1. Dupuis, S., and Merchant, S.S. (2023). Chlamydomonas reinhardtii: a model for photosynthesis and so much more. Nat Methods *20*, 1441–1442. 10.1038/s41592-023-02023-6.
2. Strenkert, D., Schmollinger, S., Gallaher, S.D., Salome, P.A., Purvine, S.O., Nicora, C.D., Mettler-Altmann, T., Soubeyrand, E., Weber, A.P.M., Lipton, M.S., et al. (2019). Multiomics resolution of molecular events during a day in the life of Chlamydomonas. Proc Natl Acad Sci U S A. 10.1073/pnas.1815238116.
3. Bišová, K., and Zachleder, V. (2014). Cell-cycle regulation in green algae dividing by multiple fission. Journal of Experimental Botany *65*, 2585–2602. 10.1093/jxb/ert466.
4. Fauser, F., Vilarrasa-Blasi, J., Onishi, M., Ramundo, S., Patena, W., Millican, M., Osaki, J., Philp, C., Nemeth, M., Salome, P.A., et al. (2022). Systematic characterization of gene function in the photosynthetic alga Chlamydomonas reinhardtii. Nat Genet *54*, 705–714. 10.1038/s41588-022-01052-9.

626 5. Merchant, S.S., Prochnik, S.E., Vallon, O., Harris, E.H., Karpowicz, S.J., Witman, G.B.,
627 Terry, A., Salamov, A., Fritz-Laylin, L.K., Marechal-Drouard, L., et al. (2007). The
628 *Chlamydomonas* genome reveals the evolution of key animal and plant functions. Science
629 *318*, 245–250.
630 6. Hoober, J.K. (1989). The Chlamydomonas Sourcebook. A Comprehensive Guide to
631 Biology and Laboratory Use. Elizabeth H. Harris. Academic Press, San Diego, CA, 1989.
632 xiv, 780 pp., illus. $145. Science *246*, 1503–1504. 10.1126/science.246.4936.1503-a.
633 7. Fussl, M., Konig, A.C., Eirich, J., Hartl, M., Kleinknecht, L., Bohne, A.V., Harzen, A.,
634 Kramer, K., Leister, D., Nickelsen, J., and Finkemeier, I. (2022). Dynamic light- and
635 acetate-dependent regulation of the proteome and lysine acetylome of Chlamydomonas.
636 Plant J *109*, 261–277. 10.1111/tpj.15555.
637 8. Boyle, N.R., and Morgan, J.A. (2009). Flux balance analysis of primary metabolism in
638 Chlamydomonas reinhardtii. BMC Syst Biol *3*, 4. 1752-0509-3-4 [pii]
639 10.1186/1752-0509-3-4.
640 9. Füßl, M., König, A.-C., Eirich, J., Hartl, M., Kleinknecht, L., Bohne, A.-V., Harzen, A.,
641 Kramer, K., Leister, D., Nickelsen, J., and Finkemeier, I. (2022). Dynamic light- and
642 acetate-dependent regulation of the proteome and lysine acetylome of Chlamydomonas.
643 The Plant Journal *109*, 261–277. https://doi.org/10.1111/tpj.15555.
644 10. Lauersen, K.J., Willamme, R., Coosemans, N., Joris, M., Kruse, O., and Remacle, C. (2016).
645 Peroxisomal microbodies are at the crossroads of acetate assimilation in the green
646 microalga Chlamydomonas reinhardtii. Algal Research *16*, 266–274.
647 https://doi.org/10.1016/j.algal.2016.03.026.

648 11. Endo, T., and Asada, K. (1996). Dark Induction of the Non-Photochemical Quenching of
649 Chlorophyll Fluorescence by Acetate in Chlamydomonas reinhardtii. Plant and Cell
650 Physiology *37*, 551–555. 10.1093/oxfordjournals.pcp.a028979.
651 12. Fett, J.P., and Coleman, J.R. (1994). Regulation of Periplasmic Carbonic Anhydrase
652 Expression in Chlamydomonas reinhardtii by Acetate and pH. Plant Physiol *106*, 103–108.
653 10.1104/pp.106.1.103.
654 13. Weger, H.G., Chadderton, A.R., Lin, M., Guy, R.D., and Turpin, D.H. (1990). Cytochrome
655 and Alternative Pathway Respiration during Transient Ammonium Assimilation by N-
656 Limited Chlamydomonas reinhardtii. Plant Physiol *94*, 1131–1136. 10.1104/pp.94.3.1131.
657 14. Weger, H.G., Guy, R.D., and Turpin, D.H. (1990). Cytochrome and alternative pathway
658 respiration in green algae : measurements using inhibitors and o(2) discrimination. Plant
659 Physiol *93*, 356–360. 10.1104/pp.93.1.356.
660 15. Kindle, K.L. (1987). Expression of a gene for a light-harvesting chlorophyll a/b-binding
661 protein in Chlamydomonas reinhardtii: effect of light and acetate. Plant Mol.Biol. *9*, 547–
662 563. 10.1007/BF00020532.
663 16. Martínez-Rivas, J.M., and Vega, J.M. (1993). Effect of culture conditions on the isocitrate
664 dehydrogenase and isocitrate lyase activities in Chlamydomonas reinhardtii. Physiologia
665 Plantarum *88*, 599–603. https://doi.org/10.1111/j.1399-3054.1993.tb01377.x.
666 17. Heifetz, P.B., Förster, B., Osmond, C.B., Giles, L.J., and Boynton, J.E. (2000). Effects of
667 Acetate on Facultative Autotrophy in Chlamydomonas reinhardtii Assessed by
668 Photosynthetic Measurements and Stable Isotope Analyses. Plant Physiology *122*, 1439–
669 1446.

670 18. Singh, H., Shukla, M.R., Chary, K.V., and Rao, B.J. (2014). Acetate and bicarbonate
671 assimilation and metabolite formation in Chlamydomonas reinhardtii: a 13C-NMR study.
672 PLoS One *9*, e106457. 10.1371/journal.pone.0106457.
673 19. Chen, J., Chen, Y., He, W., Liang, H., Hong, T., Li, T., and Du, H. (2024). Transcriptome
674 analysis reveals the molecular mechanism of differences in growth between
675 photoautotrophy and heterotrophy in Chlamydomonas reinhardtii. Frontiers in Plant
676 Science *Volume 15 - 2024*. 10.3389/fpls.2024.1407915.
677 20. Koley, S., Foley, K., Perrine, Z., Morley, S.A., Kambhampati, S., Gomez, O., Chu, K.L.,
678 Chou, Y.H., Wei, M., Tzeng, S.C., et al. (2026). Metabolic rewiring and biomass
679 redistribution enable optimized mixotrophic growth in Chlamydomonas. Proc Natl Acad
680 Sci U S A *123*, e2522572123. 10.1073/pnas.2522572123.
681 21. Kaur, S., Hérault, J., Caruso, A., Pencréac'h, G., Come, M., Gauvry, L., Claverol, S., and
682 Loiseau, C. (2021). Proteomics and expression studies on lipids and fatty acids metabolic
683 genes in Isochrysis galbana under the combined influence of nitrogen starvation and sodium
684 acetate supplementation. Bioresource Technology Reports *15*, 100714.
685 https://doi.org/10.1016/j.biteb.2021.100714.
686 22. Castaño-Cerezo, S., Bernal, V., Post, H., Fuhrer, T., Cappadona, S., Sánchez-Díaz, N.C.,
687 Sauer, U., Heck, A.J., Altelaar, A.F., and Cánovas, M. (2014). Protein acetylation affects
688 acetate metabolism, motility and acid stress response in Escherichia coli. Mol Syst Biol *10*,
689 762. 10.15252/msb.20145227.
690 23. Cross, F.R., and Umen, J.G. (2015). The *Chlamydomonas* cell cycle. The Plant Journal *82*,
691 370–392. 10.1111/tpj.12795.

692 24. Vítová, M., Bišová, K., Umysová, D., Hlavová, M., Kawano, S., Zachleder, V., and Čížková,
693 M. (2011). *Chlamydomonas reinhardtii*: duration of its cell cycle and phases at growth rates
694 affected by light intensity. Planta *233*, 75–86. 10.1007/s00425-010-1282-y.
695 25. Liu, D., Vargas-Garcia, C.A., Singh, A., and Umen, J. (2023). A cell-based model for size
696 control in the multiple fission alga Chlamydomonas reinhardtii. Curr Biol *33*, 5215–5224
697 e5215. 10.1016/j.cub.2023.10.023.
698 26. Harris, E.H. (2001). *Chlamydomonas* as a model organism. Annu Rev Plant Physiol Plant
699 Mol Biol *52*, 363–406.
700 27. Hlavová, M., Vítová, M., and Bišová, K. (2016). Synchronization of green algae by light
701 and dark regimes for cell cycle and cell division studies. In Plant Cell Division, M.-C.
702 Caillaud, ed. (Springer Science), pp. 3–16.
703 28. Coleman, A. (2004). The nuclear cell cycle in Chlamydomonas (Chlorophyceae). Journal
704 of Phycology *18*, 192–195. 10.1111/j.1529-8817.1982.tb03172.x.
705 29. Gorman, D.S., and Levine, R.P. (1965). Cytochrome f and plastocyanin: their sequence in
706 the photosynthetic electron transport chain of *Chlamydomonas reinhardi*. P. Natl. Acad. Sci.
707 USA *54*, 1665–1669.
708 30. Burgess, S.J., Taha, H., Yeoman, J.A., Iamshanova, O., Chan, K.X., Boehm, M., Behrends,
709 V., Bundy, J.G., Bialek, W., Murray, J.W., and Nixon, P.J. (2016). Identification of the
710 Elusive Pyruvate Reductase of Chlamydomonas reinhardtii Chloroplasts. Plant Cell Physiol
711 *57*, 82–94. 10.1093/pcp/pcv167.
712 31. Kselíková, V., Zachleder, V., and Bišová, K. (2022). Analysis of commitment point
713 attainment in algae dividing by multiple fission. In Plant Cell Division, M.-C. Caillaud, ed.
714 (Springer US). 10.1007/978-1-0716-1744-1_5.

32. Neumann, G., Teras, R., Monson, L., Kivisaar, M., Schauer, F., and Heipieper, H.J. (2004). Simultaneous degradation of atrazine and phenol by Pseudomonas sp. strain ADP: effects of toxicity and adaptation. Appl Environ Microbiol *70*, 1907–1912. 10.1128/aem.70.4.1907-1912.2004.

33. Brányiková, I., Maršálková, B., Doucha, J., Brányik, T., Bišová, K., Zachleder, V., and Vítová, M. (2011). Microalgae-novel highly efficient starch producers. Biotechnol. Bioeng. *108*, 766–776. 10.1002/Bit.23016.

34. Genty, B., Briantais, J.-M., and Baker, N.R. (1989). The relationship between the quantum yield of photosynthetic electron transport and quenching of chlorophyll fluorescence. Biochimica et Biophysica Acta (BBA) - General Subjects *990*, 87–92. https://doi.org/10.1016/S0304-4165(89)80016-9.

35. Wanka, F. (1962). Die bestimmung der nucleinsäuren in *Chlorella pyrenoidosa*. Planta *58*, 594–619.

36. Lukavský, J., Tetík, K., and Vendlová, J. (1973). Extraction of nucleic acid from the alga *Scenedesmus quadricauda.* Archive für Hydrobiologie, Supplement 41, Algological Studies *9*, 416–426.

37. Decallonne, J.R., and Weyns, J.C. (1976). A shortened procedure of the diphenylamine reaction for the measurement of deoxyribonucleic acid by using light activation. Analytical Biochemistry *74*, 448–456. https://doi.org/10.1016/0003-2697(76)90225-6.

38. Zachleder, V. (1984). Optimization of nucleic acids assay in green and blue-green algae: Extraction procedures and the light-activated reaction for DNA. Archive für Hydrobiologie, Supplement 67, Algological Studies *36*, 313–328.

39. Mielczarek, O., Rogers, C.H., Zhan, Y., Matheson, L.S., Stubbington, M.J.T., Schoenfelder, S., Bolland, D.J., Javierre, B.M., Wingett, S.W., Várnai, C., et al. (2023). Intra- and

739 interchromosomal contact mapping reveals the Igh locus has extensive conformational
740 heterogeneity and interacts with B-lineage genes. Cell Rep *42*, 113074.
741 10.1016/j.celrep.2023.113074.
742 40. Chen, S. (2023). Ultrafast one-pass FASTQ data preprocessing, quality control, and
743 deduplication using fastp. iMeta *2*, e107. https://doi.org/10.1002/imt2.107.
744 41. Craig, R.J., Gallaher, S.D., Shu, S., Salomé, P.A., Jenkins, J.W., Blaby-Haas, C.E., Purvine,
745 S.O., O'Donnell, S., Barry, K., Grimwood, J., et al. (2022). The Chlamydomonas Genome
746 Project, version 6: Reference assemblies for mating-type plus and minus strains reveal
747 extensive structural mutation in the laboratory. The Plant Cell *35*, 644–672.
748 10.1093/plcell/koac347.
749 42. Patro, R., Duggal, G., Love, M.I., Irizarry, R.A., and Kingsford, C. (2017). Salmon provides
750 fast and bias-aware quantification of transcript expression. Nature Methods *14*, 417–419.
751 10.1038/nmeth.4197.
752 43. Chen, Y., Chen, L., Lun, A.T.L., Baldoni, P.L., and Smyth, G.K. (2025). edgeR v4: powerful
753 differential analysis of sequencing data with expanded functionality and improved support
754 for small counts and larger datasets. Nucleic Acids Res *53*. 10.1093/nar/gkaf018.
755 44. Love, M.I., Huber, W., and Anders, S. (2014). Moderated estimation of fold change and
756 dispersion for RNA-seq data with DESeq2. Genome Biology *15*, 550. 10.1186/s13059-014-
757 0550-8.
758 45. Usadel, B., Poree, F., Nagel, A., Lohse, M., Czedik-Eysenberg, A., and Stitt, M. (2009). A
759 guide to using MapMan to visualize and compare Omics data in plants: a case study in the
760 crop species, Maize. Plant Cell Environ *32*, 1211–1229. 10.1111/j.1365-3040.2009.01978.x.

761 46. Guerrero, S., Roces, V., García-Campa, L., Valledor, L., and Meijón, M. (2024). Proteomic
762 dynamics revealed sex-biased responses to combined heat-drought stress in Marchantia.
763 Journal of Integrative Plant Biology *66*, 2226–2241. https://doi.org/10.1111/jipb.13753.
764 47. Minhas, A.K., Hodgson, P., Barrow, C.J., and A., A. (2016). A review on the assessment of
765 stress conditions for simultaneous production of microalgal lipids and carotenoids.
766 Frontiers in Microbiology *7*, 1–19. 10.3389/fmicb.2016.00546.
767 48. Baker, N.R. (2008). Chlorophyll fluorescence: a probe of photosynthesis in vivo. Annu Rev
768 Plant Biol *59*, 89–113. 10.1146/annurev.arplant.59.032607.092759.
769 49. Roach, T., Sedoud, A., and Krieger-Liszkay, A. (2013). Acetate in mixotrophic growth
770 medium affects photosystem II in Chlamydomonas reinhardtii and protects against
771 photoinhibition. Biochim Biophys Acta *1827*, 1183–1190. 10.1016/j.bbabio.2013.06.004.
772 50. Sá-Pessoa, J., Paiva, S., Ribas, D., Silva, Inês J., Viegas, Sandra C., Arraiano, Cecília M.,
773 and Casal, M. (2013). SATP (YaaH), a succinate–acetate transporter protein in Escherichia
774 coli. Biochemical Journal *454*, 585–595. 10.1042/bj20130412.
775 51. Qiu, B., Xia, B., Zhou, Q., Lu, Y., He, M., Hasegawa, K., Ma, Z., Zhang, F., Gu, L., Mao,
776 Q., et al. (2018). Succinate-acetate permease from Citrobacter koseri is an anion channel
777 that unidirectionally translocates acetate. Cell Res *28*, 644–654. 10.1038/s41422-018-0032-
778 8.
779 52. Paiva, S., Devaux, F., Barbosa, S., Jacq, C., and Casal, M. (2004). Ady2p is essential for
780 the acetate permease activity in the yeast Saccharomyces cerevisiae. Yeast *21*, 201–210.
781 10.1002/yea.1056.
782 53. Robellet, X., Flipphi, M., Pégot, S., MacCabe, Andrew P., and Vélot, C. (2008). AcpA, a
783 member of the GPR1/FUN34/YaaH membrane protein family, is essential for acetate

784 permease activity in the hyphal fungus Aspergillus nidulans. Biochemical Journal *412*,
785 485–493. 10.1042/bj20080124.
786 54. Durante, L., Hubner, W., Lauersen, K.J., and Remacle, C. (2019). Characterization of the
787 GPR1/FUN34/YaaH protein family in the green microalga Chlamydomonas suggests their
788 role as intracellular membrane acetate channels. Plant Direct *3*, e00148. 10.1002/pld3.148.
789 55. Johnson, X., and Alrica, J. (2013). Central carbon metabolism and electron transport in
790 *Chlamydomonas reinhardtii:* Metabolic constraints for carbon partitioning between oil and
791 starch. Eukaryotic Cell *12*, 776–793.
792 56. Zhou, Y., Wu, F., Wu, J., Overmans, S., Ye, M., Xiao, M., Peng, B., Xu, L., Huang, J., Lu,
793 Y., et al. (2024). The adaptive mechanisms of the marine diatom Thalassiosira weissflogii
794 to long-term high CO(2) and warming. Plant J *119*, 2001–2020. 10.1111/tpj.16905.
795 57. Kruger, N.J., and von Schaewen, A. (2003). The oxidative pentose phosphate pathway:
796 structure and organisation. Curr Opin Plant Biol *6*, 236–246. 10.1016/s1369-
797 5266(03)00039-6.
798 58. Launay, A., Cabassa-Hourton, C., Eubel, H., Maldiney, R., Guivarc'h, A., Crilat, E.,
799 Planchais, S., Lacoste, J., Bordenave-Jacquemin, M., Clement, G., et al. (2019). Proline
800 oxidation fuels mitochondrial respiration during dark-induced leaf senescence in
801 Arabidopsis thaliana. J Exp Bot *70*, 6203–6214. 10.1093/jxb/erz351.
802 59. Bisova, K., Krylov, D.M., and Umen, J.G. (2005). Genome-wide annotation and expression
803 profiling of cell cycle regulatory genes in *Chlamydomonas reinhardtii*. Plant Physiology
804 *137*, 475–491.
805 60. Zones, J.M., Blaby, I.K., Merchant, S.S., and Umen, J.G. (2015). High-resolution profiling
806 of a synchronized diurnal transcriptome from *Chlamydomonas reinhardtii* reveals

807 continuous cell and metabolic differentiation. Plant Cell *10*, 2743–2769.
808 10.1105/tpc.15.00498.
809 61. Cross, F.R. (2015). The Chlamydomonas cell cycle. The Plant Journal *82*.
810 10.1111/tpj.12795.
811 62. Magyar, Z., Meszaros, T., Miskolczi, P., Deak, M., Feher, A., Brown, S., Kondorosi, E.,
812 Athanasiadis, A., Pongor, S., Bilgin, M., et al. (1997). Cell cycle phase specificity of
813 putative cyclin-dependent kinase variants in synchronized alfalfa cells. Plant Cell *9*, 223–
814 235.
815 63. Menges, M., Hennig, L., Gruissem, W., and Murray, J.A. (2002). Cell cycle-regulated gene
816 expression in Arabidopsis. J Biol Chem *277*, 41987–42002. 10.1074/jbc.M207570200.
817 64. Olson, B.J.S.C., Oberholzer, M., Li, Y.B., Zones, J.M., Kohli, H.S., Bisova, K., Fang, S.C.,
818 Meisenhelder, J., Hunter, T., and Umen, J.G. (2010). Regulation of the *Chlamydomonas*
819 cell cycle by a stable, chromatin-associated retinoblastoma tumor suppressor complex.
820 Plant Cell *22*, 3331–3347. 10.1105/tpc.110.076067.
821 65. Atkins, K.C., and Cross, F. (2018). Inter-regulation of CDKA/CDK1 and the plant-specific
822 cyclin-dependent kinase CDKB in control of the *Chlamydomonas* cell cycle. Plant Cell *30*,
823 429–446. 10.1105/tpc.17.00759.
824 66. De Schutter, K., Joubes, J., Cools, T., Verkest, A., Corellou, F., Babiychuk, E., Van Der
825 Schueren, E., Beeckman, T., Kushnir, S., Inze, D., and De Veylder, L. (2007). Arabidopsis
826 WEE1 kinase controls cell cycle arrest in response to activation of the DNA integrity
827 checkpoint. Plant Cell *19*, 211–225.
828 67. Rai, M.P., Nigam, S., and Sharma, R. (2013). Response of growth and fatty acid
829 compositions of Chlorella pyrenoidosa under mixotrophic cultivation with acetate and

830 glycerol for bioenergy application. Biomass and Bioenergy *58*, 251–257.
831 https://doi.org/10.1016/j.biombioe.2013.08.038.
832 68. Smith, R.T., Bangert, K., Wilkinson, S.J., and Gilmour, D.J. (2015). Synergistic carbon
833 metabolism in a fast growing mixotrophic freshwater microalgal species Micractinium
834 inermum. Biomass and Bioenergy *82*, 73–86.
835 https://doi.org/10.1016/j.biombioe.2015.04.023.
836 69. Singh, S.P., and Singh, P. (2014). Effect of CO2 concentration on algal growth: A review.
837 Renewable and Sustainable Energy Reviews *38*, 172–179. 10.1016/j.rser.2014.05.043.
838 70. Gao, Y., Li, Y., Yang, Y., Feng, J., Ji, L., and Xie, S. (2023). Effects of Trophic Modes on
839 the Lipid Accumulation of Parachlorella kessleri TY. Fermentation *9*, 891.
840 71. Bialevich, V., Zachleder, V., and Bišová, K. (2022). The effect of variable light source and
841 light intensity on the growth of three algal species. Cells *11*, 1293. 10.3390/cells11081293.
842 72. Murata, N., Takahashi, S., Nishiyama, Y., and Allakhverdiev, S.I. (2007). Photoinhibition
843 of photosystem II under environmental stress. Biochimica et Biophysica Acta (BBA) -
844 Bioenergetics *1767*, 414–421. https://doi.org/10.1016/j.bbabio.2006.11.019.
845 73. Cheirsilp, B., and Torpee, S. (2012). Enhanced growth and lipid production of microalgae
846 under mixotrophic culture condition: effect of light intensity, glucose concentration and fed-
847 batch cultivation. Bioresour Technol *110*, 510–516. 10.1016/j.biortech.2012.01.125.
848 74. Kroymann, J., Schneider, W., and Zetsche, K. (1995). Opposite Regulation of the Copy
849 Number and the Expression of Plastid and Mitochondrial Genes by Light and Acetate in
850 the Green Flagellate Chlorogonium. Plant Physiology *108*, 1641–1646.
851 10.1104/pp.108.4.1641.

852 75. Wilken, S., Huisman, J., Naus-Wiezer, S., and Van Donk, E. (2013). Mixotrophic organisms
853 become more heterotrophic with rising temperature. Ecol Lett *16*, 225–233.
854 10.1111/ele.12033.
855 76. Eppley, R.W., and MaciasR, F.M. (1963). ROLE OF THE ALGA CHLAMYDOMONAS
856 MUNDANA IN ANAEROBIC WASTE STABILIZATION LAGOONS. Limnology and
857 Oceanography *8*, 411–416. https://doi.org/10.4319/lo.1963.8.4.0411.
858 77. Zhang, H., Zhao, L., Chen, Y., Zhu, M., Xu, Q., Wu, M., Han, D., and Hu, Q. (2021).
859 Trophic Transition Enhanced Biomass and Lipid Production of the Unicellular Green Alga
860 Scenedesmus acuminatus. Front Bioeng Biotechnol *9*, 638726. 10.3389/fbioe.2021.638726.
861 78. Recuenco-Munoz, L., Offre, P., Valledor, L., Lyon, D., Weckwerth, W., and Wienkoop, S.
862 (2015). Targeted quantitative analysis of a diurnal RuBisCO subunit expression and
863 translation profile in Chlamydomonas reinhardtii introducing a novel Mass Western
864 approach. J Proteomics *113*, 143–153. 10.1016/j.jprot.2014.09.026.
865 79. Boyle, N.R., Sengupta, N., and Morgan, J.A. (2017). Metabolic flux analysis of
866 heterotrophic growth in Chlamydomonas reinhardtii. PLoS One *12*, e0177292.
867 10.1371/journal.pone.0177292.
868 80. Hayashi, Y., Sato, N., Shinozaki, A., and Watanabe, M. (2015). Increase in peroxisome
869 number and the gene expression of putative glyoxysomal enzymes in Chlamydomonas cells
870 supplemented with acetate. Journal of Plant Research *128*, 177–185. 10.1007/s10265-014-
871 0681-8.
872 81. Plancke, C., Vigeolas, H., Hohner, R., Roberty, S., Emonds-Alt, B., Larosa, V., Willamme,
873 R., Duby, F., Onga Dhali, D., Thonart, P., et al. (2014). Lack of isocitrate lyase in
874 Chlamydomonas leads to changes in carbon metabolism and in the response to oxidative
875 stress under mixotrophic growth. Plant J *77*, 404–417. 10.1111/tpj.12392.

876 82. Xie, X., Huang, A., Gu, W., Zang, Z., Pan, G., Gao, S., He, L., Zhang, B., Niu, J., Lin, A.,
877 and Wang, G. (2015). Photorespiration participates in the assimilation of acetate in
878 Chlorella sorokiniana under high light. New Phytologist, n/a–n/a. 10.1111/nph.13659.
879 83. Pick, T.R., Bräutigam, A., Schulz, M.A., Obata, T., Fernie, A.R., and Weber, A.P. (2013).
880 PLGG1, a plastidic glycolate glycerate transporter, is required for photorespiration and
881 defines a unique class of metabolite transporters. Proc Natl Acad Sci U S A *110*, 3185–3190.
882 10.1073/pnas.1215142110.
883 84. Chapman, S.P., Paget, C.M., Johnson, G.N., and Schwartz, J.M. (2016). Corrigendum: Flux
884 balance analysis reveals acetate metabolism modulates cyclic electron flow and alternative
885 glycolytic pathways in Chlamydomonas reinhardtii. Front Plant Sci *7*, 362.
886 10.3389/fpls.2016.00362.
887 85. Zuniga, C., Li, C.T., Huelsman, T., Levering, J., Zielinski, D.C., McConnell, B.O., Long,
888 C.P., Knoshaug, E.P., Guarnieri, M.T., Antoniewicz, M.R., et al. (2016). Genome-scale
889 metabolic model for the green alga Chlorella vulgaris UTEX 395 accurately predicts
890 phenotypes under autotrophic, heterotrophic, and mixotrophic growth conditions. Plant
891 Physiol. 10.1104/pp.16.00593.
892 86. von Gromoff, E.D., Treier, U., and Beck, C.F. (1989). Three light-inducible heat shock
893 genes of Chlamydomonas reinhardtii. Molecular and cellular biology *9*, 3911–3918.
894 10.1128/MCB.9.9.3911.
895 87. Schroda, M., Vallon, O., Wollman, F.A., and Beck, C.F. (1999). A chloroplast-targeted heat
896 shock protein 70 (HSP70) contributes to the photoprotection and repair of photosystem II
897 during and after photoinhibition. Plant Cell *11*, 1165–1178.

898 88. Kropat, J., von Gromoff, E.D., Müller, F.W., and Beck, C.F. (1995). Heat shock and light
899 activation of a Chlamydomonas HSP70 gene are mediated by independent regulatory
900 pathways. Mol Gen Genet *248*, 727–734. 10.1007/bf02191713.
901 89. Schuster, G., Even, D., Kloppstech, K., and Ohad, I. (1988). Evidence for protection by
902 heat-shock proteins against photoinhibition during heat-shock. Embo j *7*, 1–6.
903 10.1002/j.1460-2075.1988.tb02776.x.
904 90. Arora, N., and Philippidis, G.P. (2021). Insights into the physiology of Chlorella vulgaris
905 cultivated in sweet sorghum bagasse hydrolysate for sustainable algal biomass and lipid
906 production. Sci Rep *11*, 6779. 10.1038/s41598-021-86372-2.
907 91. Choi, B.Y., Kim, H., Shim, D., Jang, S., Yamaoka, Y., Shin, S., Yamano, T., Kajikawa, M.,
908 Jin, E., Fukuzawa, H., and Lee, Y. (2022). The Chlamydomonas bZIP transcription factor
909 BLZ8 confers oxidative stress tolerance by inducing the carbon-concentrating mechanism.
910 Plant Cell *34*, 910–926. 10.1093/plcell/koab293.
911 92. Ji, C., Mao, X., Hao, J., Wang, X., Xue, J., Cui, H., and Li, R. (2018). Analysis of bZIP
912 Transcription Factor Family and Their Expressions under Salt Stress in Chlamydomonas
913 reinhardtii. Int J Mol Sci *19*. 10.3390/ijms19092800.
914 93. Boonyaves, K., Wu, T.Y., Dong, Y., and Urano, D. (2022). Interplay between
915 ARABIDOPSIS Gbeta and WRKY transcription factors differentiates environmental stress
916 responses. Plant Physiol *190*, 813–827. 10.1093/plphys/kiac305.
917 94. Wang, W., Cao, H., Wang, J., and Zhang, H. (2024). Recent advances in functional assays
918 of WRKY transcription factors in plant immunity against pathogens. Front Plant Sci *15*,
919 1517595. 10.3389/fpls.2024.1517595.

95. Lin, Y.T., Takeuchi, T., Youk, B., Umen, J., Sears, B.B., and Benning, C. (2022). Chlamydomonas CHT7 is involved in repressing DNA replication and mitotic genes during synchronous growth. G3 (Bethesda) *12*. 10.1093/g3journal/jkac023.

96. Takeuchi, T., Sears, B.B., Lindeboom, C., Lin, Y.T., Fekaris, N., Zienkiewicz, K., Zienkiewicz, A., Poliner, E., and Benning, C. (2020). Chlamydomonas CHT7 Is Required for an Effective Quiescent State by Regulating Nutrient-Responsive Cell Cycle Gene Expression. Plant Cell *32*, 1240–1269. 10.1105/tpc.19.00628.

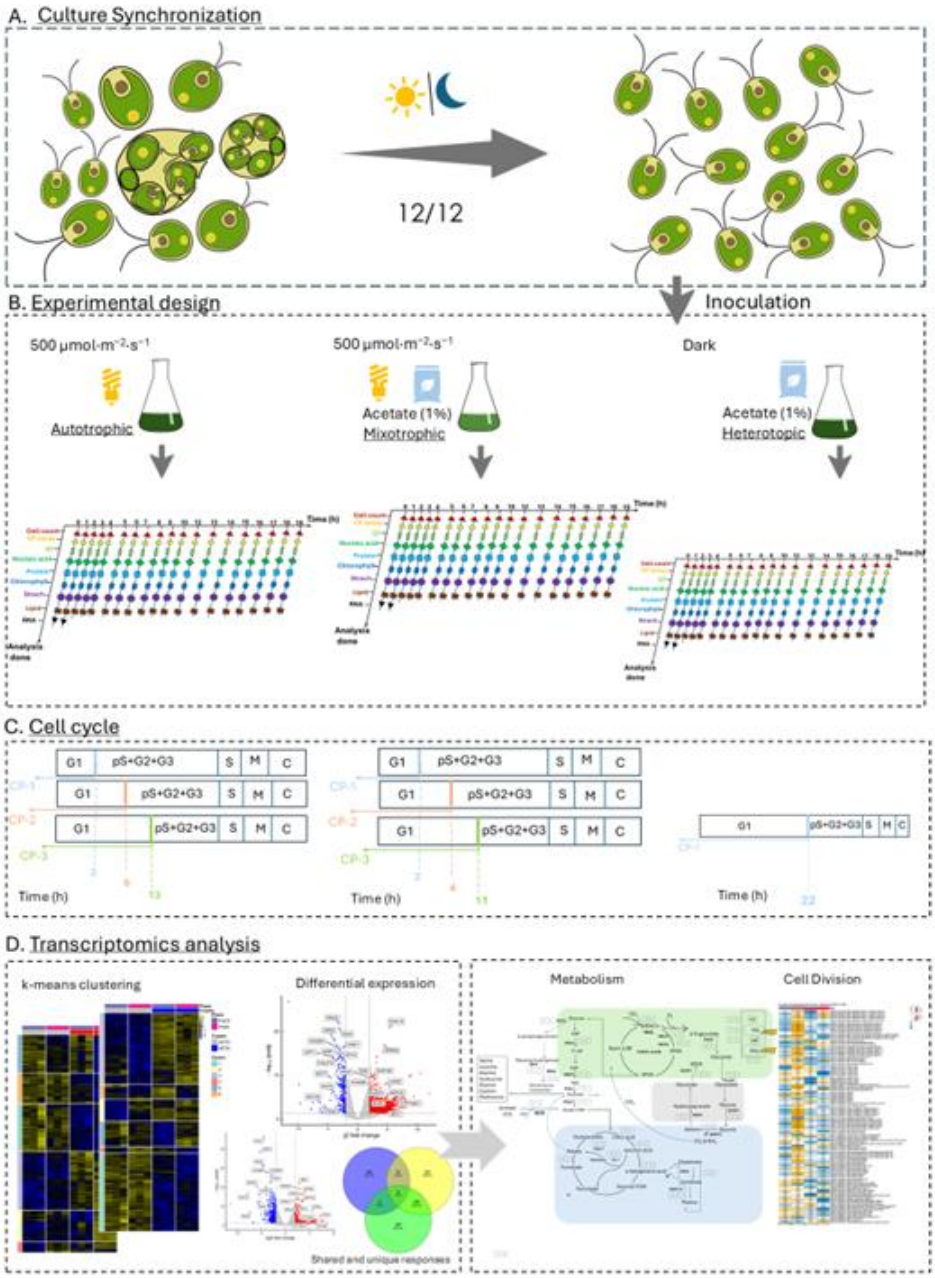

930 **Figure 1.** Schematic representation of the experimental design. A) *Chlamydomonas reinhardtii*
931 cultures were synchronized using 12 h light/12 h dark cycles at 30 °C and an irradiance of 500
932 µmol m^{-2} s^{-1}. B) For the experiment, synchronized cells were diluted to approximately 1×10^6 cells
933 mL^{-1} in HSM (AUTO) or TAP (MIXO, HETERO) and grown at 30 °C under continuous light (500
934 µmol m^{-2} s^{-1} PAR), bubbled with 2% CO_2 in air. Experiments were performed in biological
935 triplicates with hourly or bi-hourly sampling for different analyses. C) Representation of cell cycle

936 events in each trophic condition. D) Schematic representation of the transcriptomics analysis
937 workflow.

938

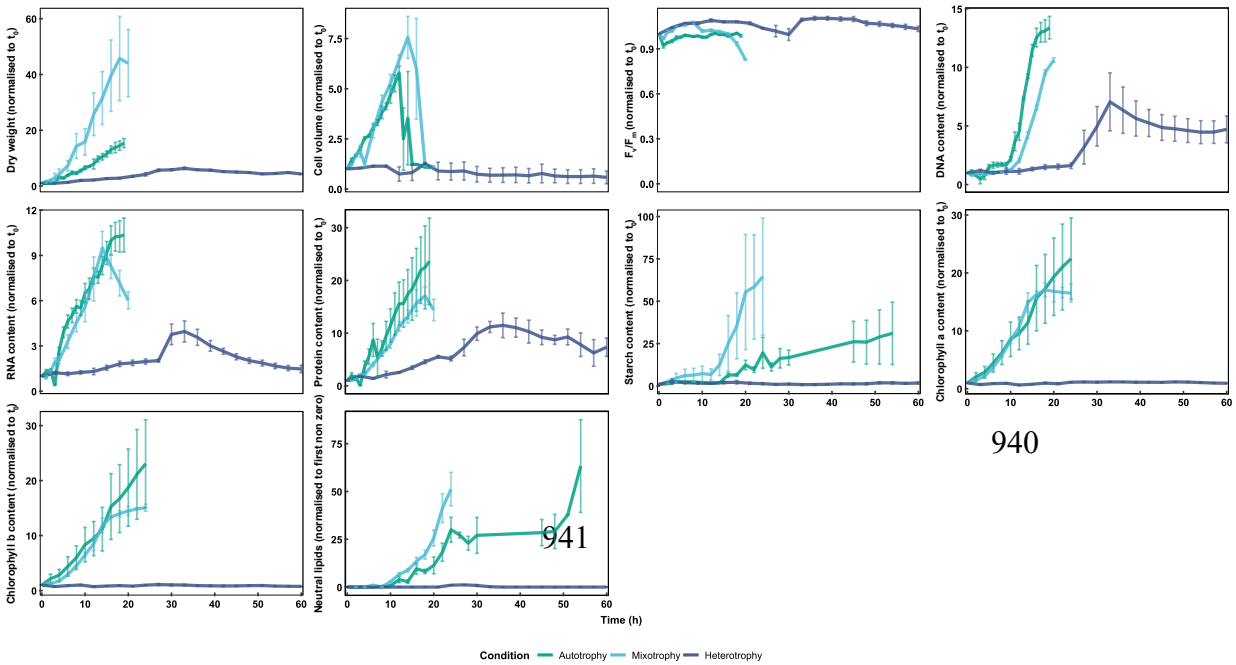

Figure 2. Growth of synchronized cultures of *C. reinhardtii* grown under different trophic regimes (a) dry cell weight, (b) changes in mean cell volume, (c) maximum quantum efficiency of photosystem II (F_v/F_m), (d) DNA, (e) RNA, (f) protein, (g) starch (pg cell^{-1}), (h) chlorophyll *a*, (i) chlorophyll *b,* (j) neutral lipids (pg cell^{-1}). All the experiment are represented as (n=3) biological replicates.

949

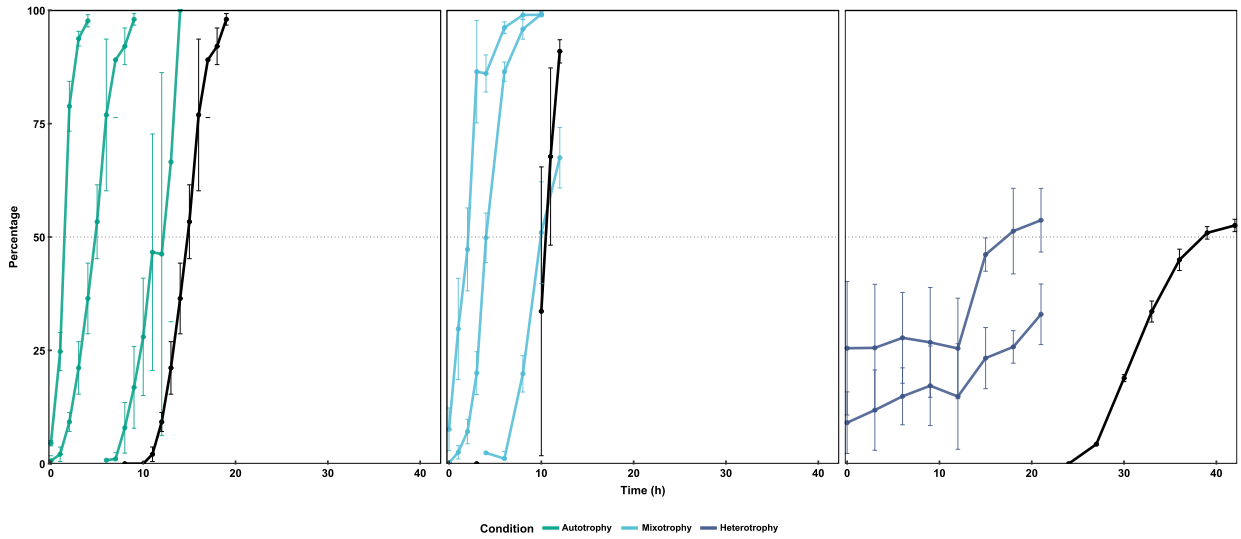

950

951 **Figure 3.** Cell cycle progression in a synchronized culture of *C. reinhardtii* grown under different
952 trophic regimes. Time courses of individual commitment points (CP, colored lines) and daughter
953 cell release (black lines) in autotrophy (A), mixotrophy (B), and heterotrophy (C). The colored
954 curves show the cumulative percentage of cells that attained the CP for division into 2 (squares), 4
955 (circles), and 8 (triangles) daughter cells. The black lines show the cumulative percentage of cells
956 that completed cell division. The gray dashed line depicts the midpoint of each event in the cell
957 population. All experiments are represented as biological replicates (n = 3).

958

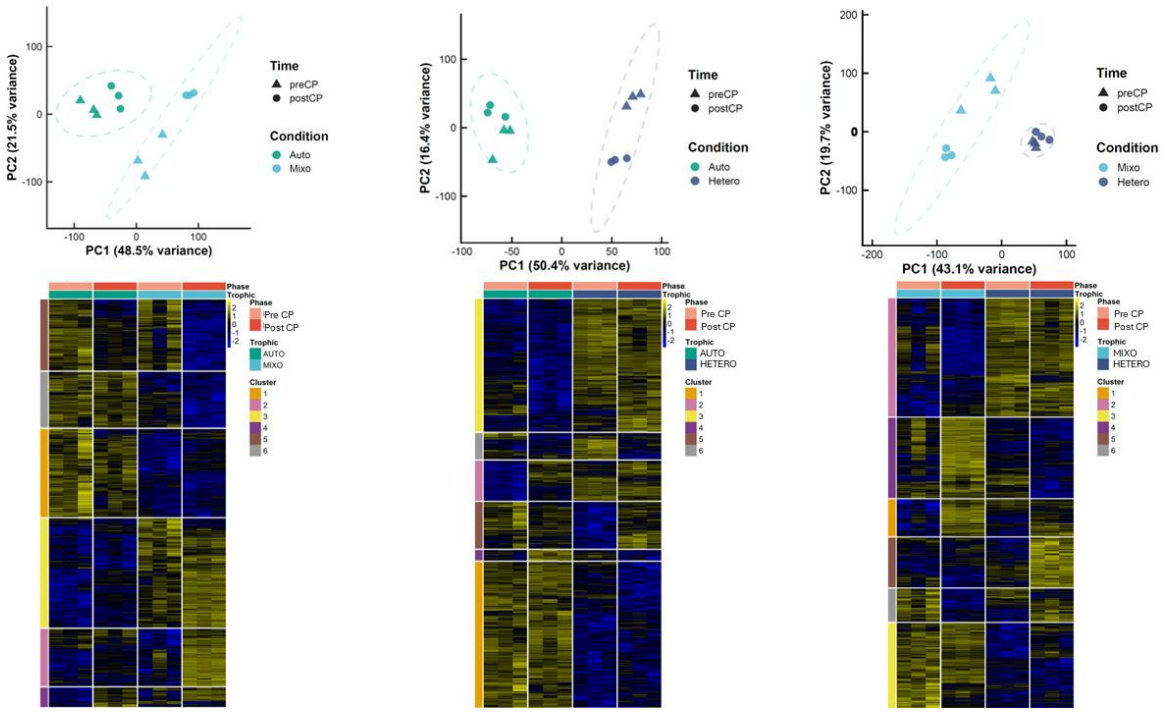

Figure 4. Principal Component Analysis (PCA) of genome-wide RNA abundances (FPKMs) across three biological replicates (n = 3). This analysis shows sample clustering based on gene expression profiles from RNA-seq data of C. reinhardtii. The first principal component (PC1) and the second principal component (PC2) are displayed. **A**, AUTO and MIXO, **B**, HETERO and AUTO, **C**, MIXO and HETERO. RNA expression was grouped into eight clusters by k-means clustering of their normalized expression patterns. Normalized values are the Z-scores of the mean mRNA abundance (FPKM) from three experimental replicates (n = 3) in **A**, AUTO and MIXO, **B**, HETERO and AUTO, and **C**, MIXO and HETERO.

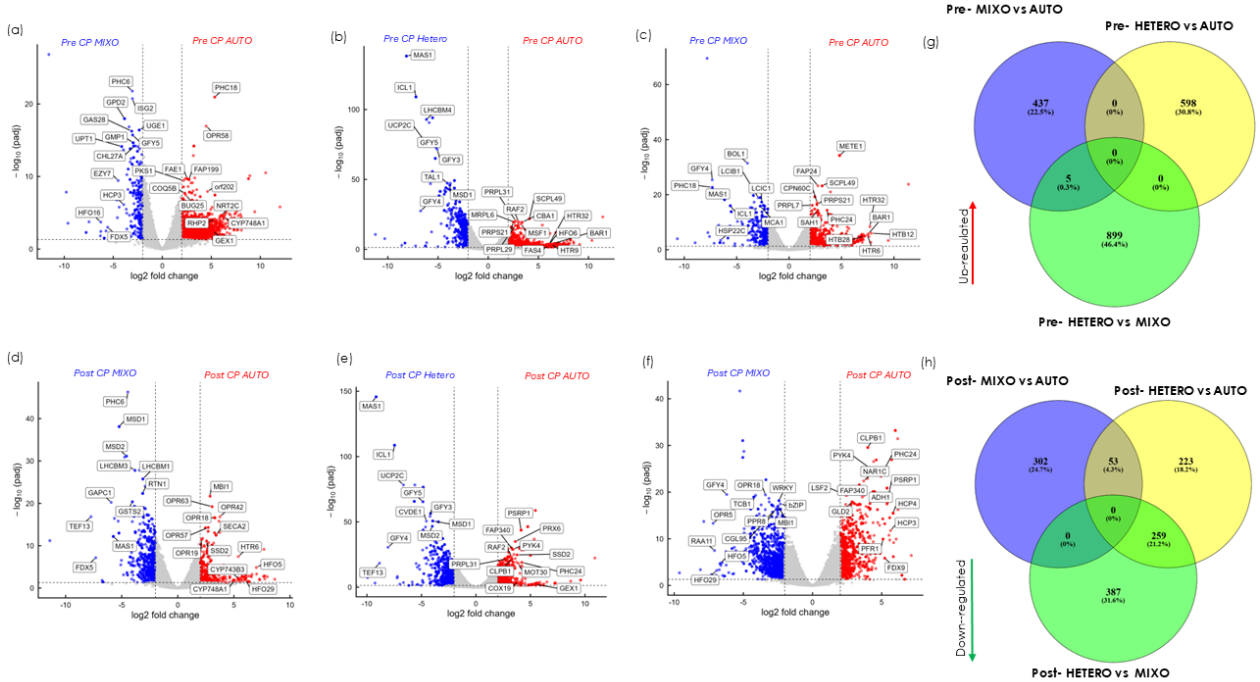

Figure 5. Differential gene expression analysis of C. reinhardtii under different growth conditions. Volcano plots show the correlation between log2(FC) values of genes and the corresponding –$\log_{10}$(padj-values); only genes quantified in three biological replicates are included. **A**, Differential gene expression analysis: Pre-CP MIXO vs. Pre-CP AUTO; **B**, Pre-CP HETERO vs. Pre-CP AUTO; **C**, Pre-CP MIXO vs. Pre-CP HETERO; **D**, Post-CP MIXO vs. Post-CP AUTO; **E**, Post-CP HETERO vs. Post-CP AUTO; **F**, Post-CP MIXO vs. Post-CP HETERO. Venn diagrams of upregulated (**G**) and downregulated (**H**) genes show the shared and unique responses among the conditions.

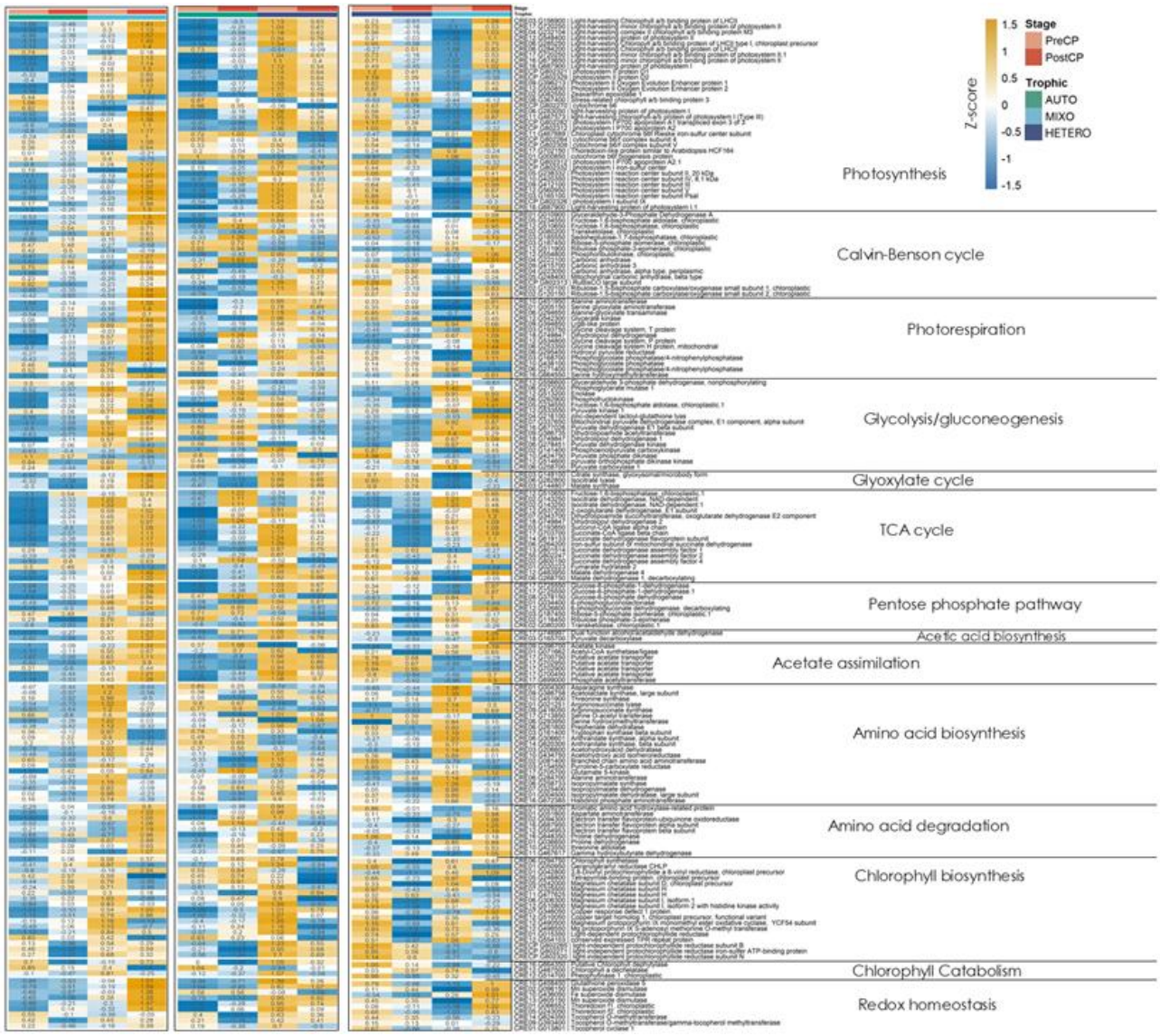

Figure 6. Z-score heatmaps show the expression of genes involved in central metabolic pathways in AUTO, MIXO, and HETERO under Pre-CP and Post-CP conditions. Colors indicate relative expression levels (yellow - increased; blue - decreased).

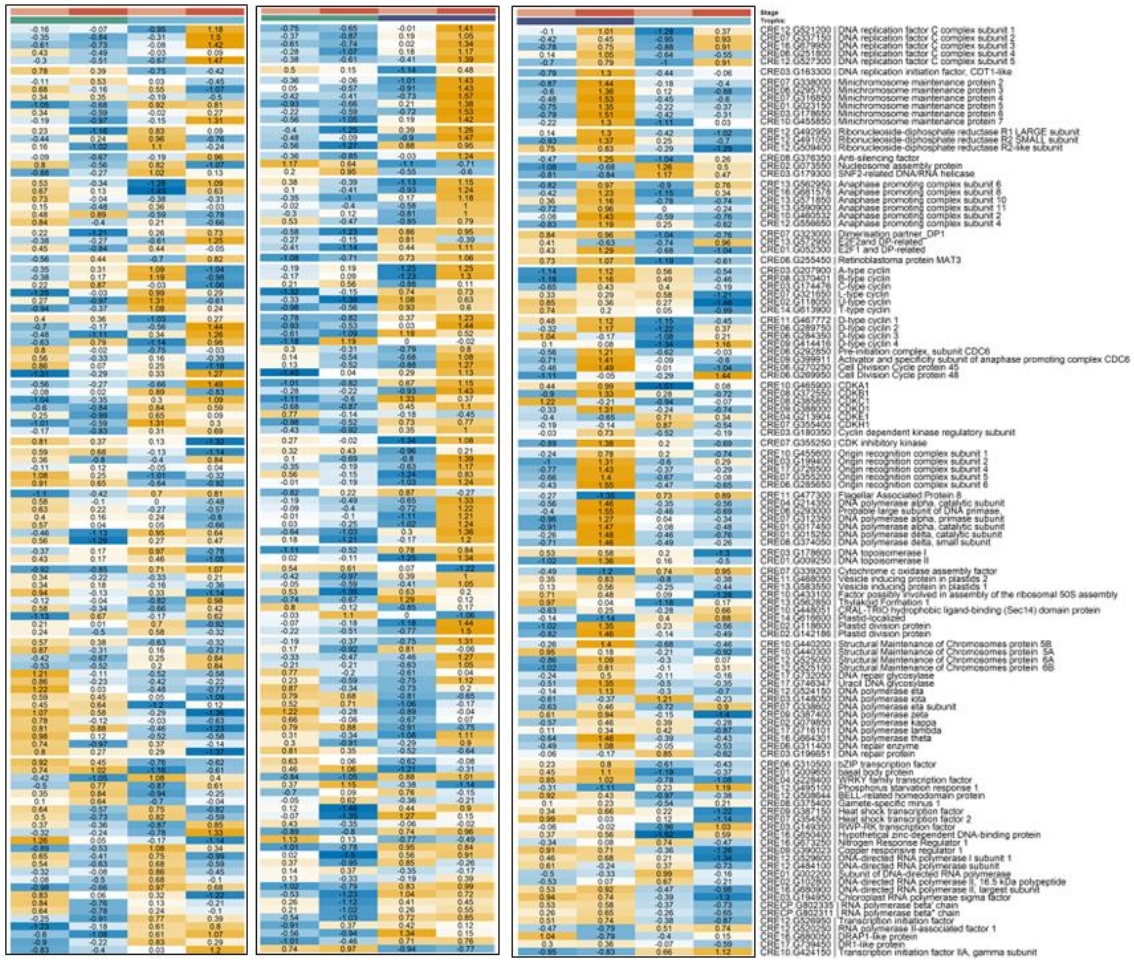

Figure 7. Z-score heatmaps show the expression of genes involved in the cell cycle in AUTO, MIXO, and HETERO under PreCP and Post-CP conditions. Colors indicate relative expression levels (yellow – increased, blue - decreased)

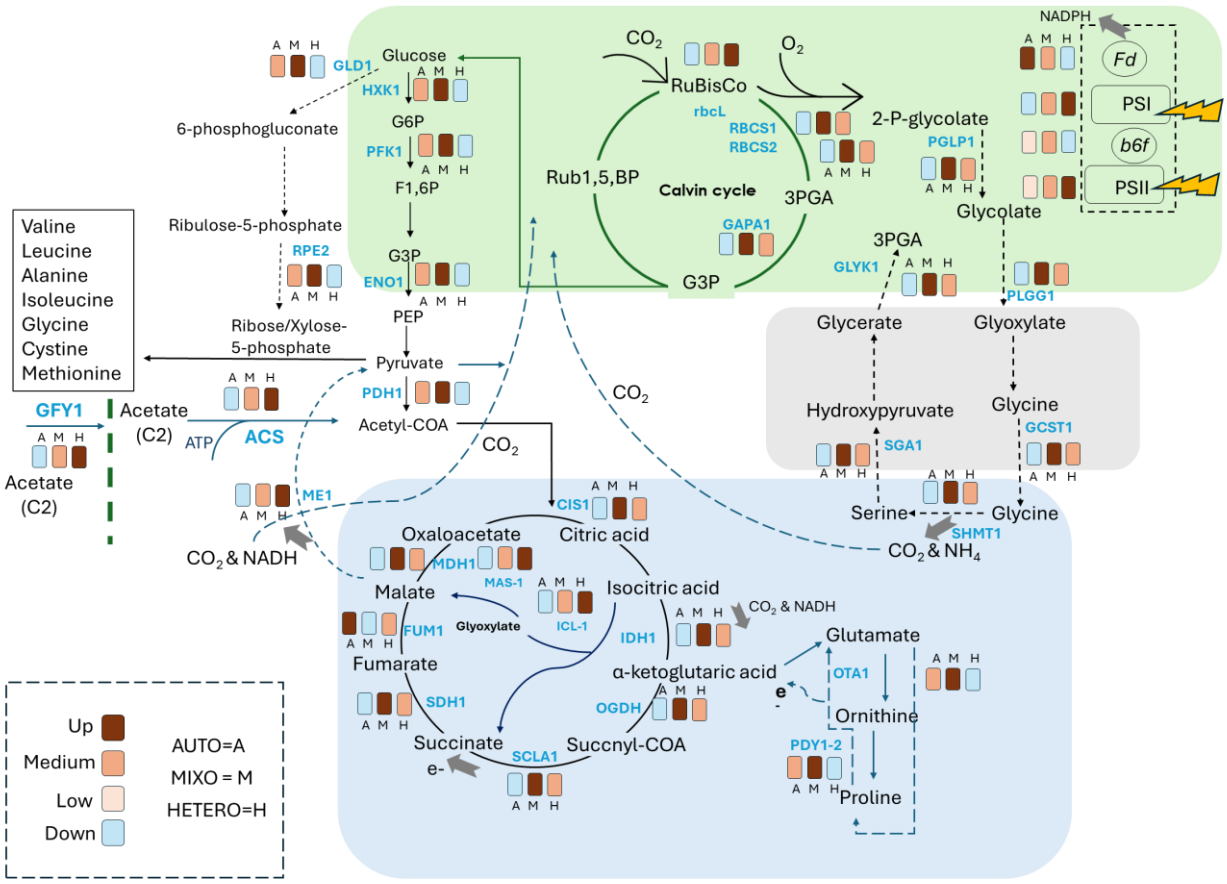

991

992 **Figure 8.** Systematic representation of metabolic changes under phototrophic, mixotrophic, and
993 heterotrophic growth conditions in *Chlamydomonas reinhardtii*, with gene expression at Post-CP
994 and CP time points shown here. *rbcL*: RuBisCO large subunit; *RBCS1*: ribulose-1,5-bisphosphate
995 carboxylase/oxygenase small subunit 1, chloroplastic; *RBCS2*: ribulose-1,5-bisphosphate
996 carboxylase/oxygenase small subunit 2, chloroplastic; *GAPA1*: glyceraldehyde-3-phosphate
997 dehydrogenase A; *PGLP1*: phosphoglycolate phosphatase; *PLGG1*: plastidic glycolate/glycerate
998 transporter; *SHMT1*: serine hydroxymethyltransferase; *SGA1*: glyoxylate aminotransferase; *GLYK*:
999 glycerate kinase; *GLD1*: glucose-6-phosphate-1-dehydrogenase; *HXK1*: hexokinase; *PFK1*:
1000 phosphofructokinase; *ENO1*: Enolase; *PDH1*: Pyruvate dehydrogenase; *RPE2*: ribulose
1001 phosphate-3-epimerase; *CIS1*: citrate synthase, mitochondrial; *IDH1*: isocitrate dehydrogenase;
1002 *OGDH*: 2-oxoglutarate dehydrogenase; *SCLA1*: succinyl-CoA ligase; *SDH1*: succinate

1003 dehydrogenase; *FUM1*: fumarate hydratase; *MDH1*: malate dehydrogenase; *ME1*: malic enzyme;

1004 *ACS*: acetyl-CoA synthetase; *GFY*: putative acetate transporter; *OTA1*: ornithine transaminase;

1005 *PDY1*: proline dehydrogenase.

1006

Time (Hour)	AUTO *(pg cell^{-1})*			MIXO *(pg cell^{-1})*			HETERO *(pg cell^{-1})*		
	DNA	*RNA*	*Protein*	*DNA*	*RNA*	*Protein*	*DNA*	*RNA*	*Protein*
0	2.06 ± 0.04	0.18 ± 0.48	10.48 ± 8.03	0.39 ± 0.07	4.52 ± 1.53	18.40 ± 5.66	1.39 ± 0.01	0.11 ± 0.08	4.62 ± 1.11
2	2.59± 0.02	0.19 ±0.50	15.58 ± 4.66	0.33 ± 0.07	5.69 ± 1.17	24.95 ± 11.63	-		-
3	0.88 ± .09	0.07 ± 0.22	0.96 ± 0.45	0.41 ± 0.05	8.35 ± 1.13	39.79 ± 11.79	1.70 ± 0.02	0.13 ± 0.24	8.51 ± 1.94
4	5.40 ± 0.12	0.15 ± 0.48	28.40 ±4.03	**0.33 ± 0.06**	**8.83 ± 1.48**	**38.64 ±7.35**	-	-	-
6	**9.29 ± 0.02**	**0.28 ± 0.55**	**64.45 ± 9.04**	0.39 ± 0.06	14.06 ± 1.60	72.98 ± 10.10	-	-	-
8	11.47 ± 0.02	0.30 ± 2.19	60.97 ± 19.87	0.42 ± 0.09	19.56 ± 2.56	108.42 ± 17.49	-	-	-
10	13.31 ± 0.03	0.38 ± 3.07	91.13 ± 11.26	**0.48 ± 0.04**	**23.76 ± 3.43**	**141.82 ± 25.44**	-	-	-
12	**15.60 ± 0.36**	**0.83 ± 2.98**	**125.00 ± 18.77**	0.79 ±0.13	31.55 ± 6.03	202.84 ± 40.51	1.83 ± 0.04	0.13 ±0.57	11.78 ± 3.03
21	-	-	-	-	-	-	**2.63 ± 0.03**	**0.17 ± 0.56**	**25.11 ± 4.57**

Table 1 Quantification of cell volume, DNA, RNA, and protein content across commitment phases (CP) in *Chlamydomonas reinhardtii* under different trophic regimes

Variant	CP time, h	CP size, µm3
AUTO	1	81.48±6.98
MIXO	2	77.59±4.98
HETERO	15	71.05±2.45

Table 2 Time of reaching commitment point and critical cell size in *Chlamydomonas reinhardtii* under different trophic regimes